Chapter 6

Data analysis

In this chapter, we describe the analysis of open-charm production in $\gamma\gamma$ collisions using the inclusive-electron method in detail.

As described in Chapter 1 and 2, we have studied the open-charm production in (quasi-)real $\gamma\gamma$ collisions:

$$e^+e^- \rightarrow (e^+e^-)c\bar{c},$$

where scattering angles of the beam electron and positron were limited to be small (less than 3.2°) to ensure the real $\gamma\gamma$-collision condition. In order to tag the c-quarks produced via two-photon processes, we identified the electron tracks from semileptonic decay of the c-quarks which have large semileptonic branching fraction of $\sim$10%. For the light quarks, only $\pi^0 \rightarrow e^+e^-(\gamma)$ and $K \rightarrow \pi e\mu$ are sources of the electrons, where we could ignore the decay of $K^{\pm}$ and K_L because of their long life time of $c\tau = 3.709$m and 15.49m, respectively. The decay of K^0_S could be also neglect due to its small branching fraction of $(6.68 \pm 0.10)\times 10^{-4}$. The π^0 decay was separated and rejected as described below. The inclusive-electron method therefore is a good tool to tag the c-quarks.

6.1 Two-photon event selection

After the whole event reconstruction described in Chapter 4, we selected the hadronic events produced by two-photon interactions.

In the TOPAZ trigger system, hadronic two-photon events were detected mainly by the charged-track trigger. The trigger required at least two charged tracks with $P_T > 0.3$ - 0.7 GeV and an opening angle > 45 - 70 degrees (depending on the beam condition) as described in the section 3.3. The trigger efficiency for

charmed events in two-photon processes was estimated with a trigger simulation to be about 93%.

In the hadronic two-photon events characterized by relatively lower visible energies than those of the e^+e^- annihilation processes, multi charged tracks and neutral clusters were produced. We selected the hadronic two-photon events using charged tracks in the TPC and neutral clusters in the BCL.

For the charged tracks in the TPC, we imposed the following conditions:

- $R_{closest} < 4.0$ cm;
- $|Z_{closest}| < 15.0$ cm;
- $P_T > 0.15$ GeV; and
- The polar angle $0.02 < |\cos\theta| < 0.83$.

Where $R_{closest}$ and $Z_{closest}$ were minimum distances of the charged tracks from the beam interaction point (I.P.) in the xy-plane and z-direction, respectively. The conditions on the $Z_{closest}$ and $R_{closest}$ selected the tracks which originated from the I.P.. We set the $Z_{closest}$ condition loosely to study the beam gas event which produced at any positions on the beam-line. $P_T = 0.15$ GeV was the minimum transverse momentum in which the track made three pad hits in the TPC. The fourth condition ensures the tracks to exist within the TPC sense volume avoiding the TPC central membrane. Figs. 6.1 show the distributions of these quantities for the experimental data.

For the neutral clusters in the BCL, we required the followings:

- $E_{BCL} > 100$ MeV; and
- The polar angle $|\cos\theta| < 0.83$.

We set the energy threshold to reject noise in the calorimeter. We imposed the condition on the polar angle to ensure the clusters surely to exist in the BCL.

We also used the neutral clusters in the ECL and the FCL only to detect the beam-electrons scattered in the large angles (ECL, FCL) and remnant-jet which produced in the beam direction predominantly (FCL). Accepted energy region in these two calorimeters are relatively high ($\sim$ 10 GeV for beam electron and $\sim$ 0.5 GeV for remnant-jet) where the performance of the detectors is expected to be well.

Using the charged tracks and the neutral clusters, two-photon events were selected based on the following criteria:

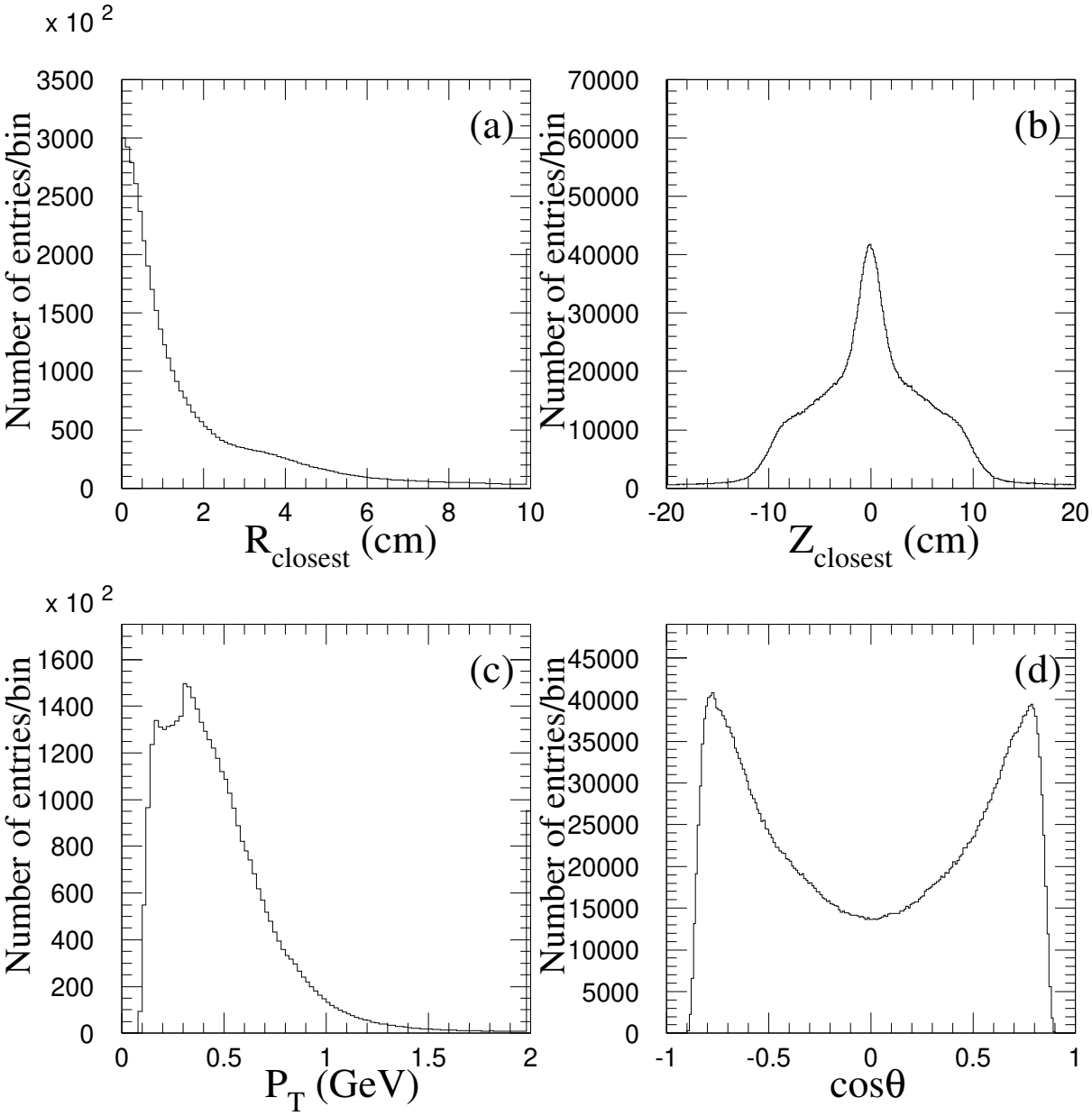

Figure 6.1: Various distributions on the track selection: (a)$R_{closest}$, (b)$Z_{closest}$, (c)P_T, and (d)$\cos\theta$.

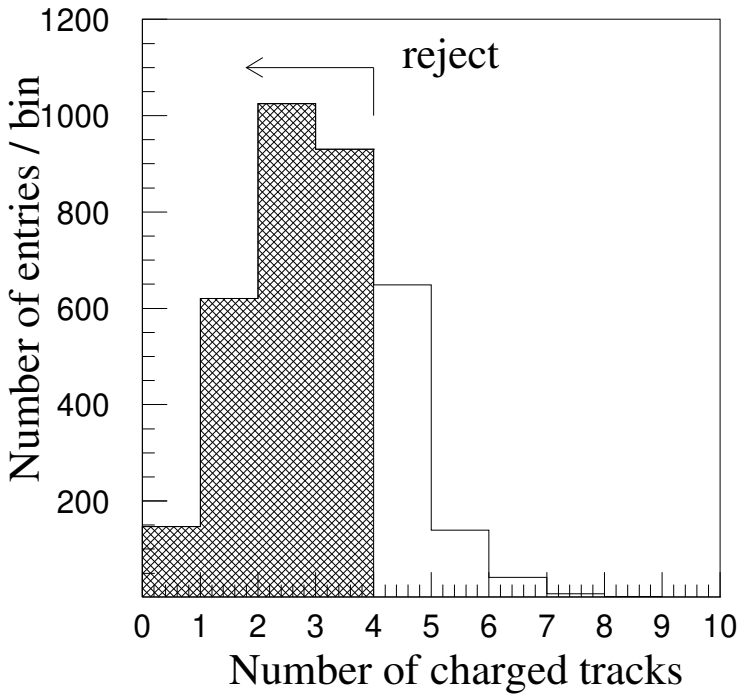

Figure 6.2: Distribution of the charged multiplicity for $e^+e^- \to (e^+e^-)\tau^+\tau^-$ events (Monte-Carlo data).

1. The number of charged tracks in the TPC has to be at least 4;
2. The visible energy ($E_{visible}$) of the event has to satisfy $E_{visible} \leq 30$ GeV;
3. The mass of the system of the observed hadrons($W_{visible}$) has to be $W_{visible} \geq 3$ GeV;
4. The position of the origin of the event(i.e. the event vertex), reconstructed from all tracks, has to be within 1.5 cm in the xy-plane and within $\pm$ 2.0 cm along the beam line from the interaction point; and
5. The energy of the most energetic cluster appearing in the BCL, the ECL, or the FCL has to be less than $0.4E_{beam}$.

In the calculation of the $E_{visible}$ and the $W_{visible}$, both the charged tracks in the TPC and the neutral clusters in the BCL are used. With the criterion 1, we rejected the low-multiplicity events such as $e^+e^- \to e^+e^-$, $\tau^+\tau^-$, and $\mu^+\mu^-$ and $e^+e^- \to (e^+e^-)e^+e^-$, $(e^+e^-)\tau^+\tau^-$, and $(e^+e^-)\mu^+\mu^-$, as shown in Fig. 6.2 which is the multiplicity distribution for $e^+e^- \to (e^+e^-)\tau^+\tau^-$ events as an example. Fig. 6.3 shows the scatter plot of the visible energy $E_{visible}$ and $E_z/E_{visible}$. A cluster at $E_{visible} \sim 2 \times E_{beam}$(=58GeV) came from e^+e^- annihilation events, while a

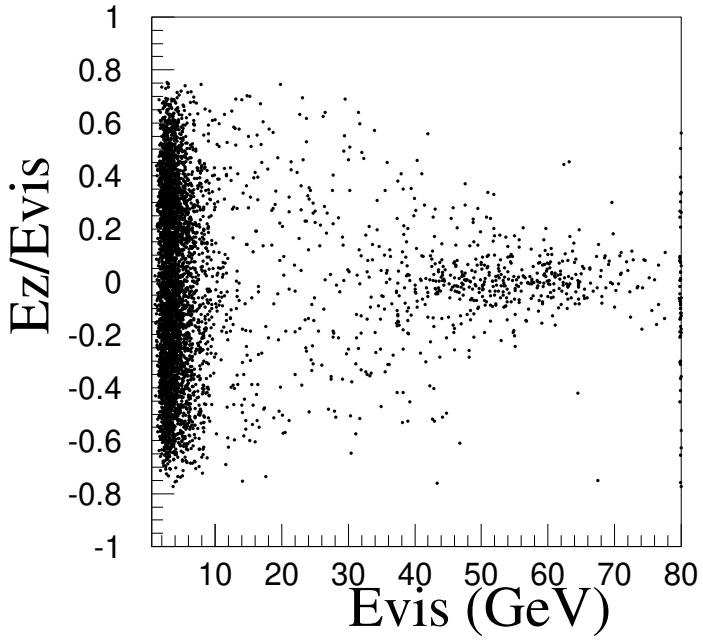

Figure 6.3: Scatter plot of $E_{visible}$ vs $E_z/E_{visible}$.

band at lower energy region from the two-photon events. Fig. 6.4 shows $E_{visible}$ distributions for the experimental data (the open histogram) and two-photon events generated by Monte-Carlo simulation (the hatched one). We could reject most of the e^+e^- annihilation events with the criterion 2, as seen in these figures. Criterion 3 remove the low-energy resonance-production events. Figs. 6.5-(a) and (b) show the W distributions for (a) $\gamma\gamma \to c\bar{c}$ events and (b) VDM events. The $c\bar{c}$ events have relatively high-W value. We also rejected the huge VDM background effectively with criterion 3. Figs. 6.6 show the vertex (a) Z and (b) R distributions. As shown in the figures, beam-gas events were produced at any positions on the beam-line. To remove the beam-gas backgrounds, we applied the vertex cuts described in the criterion 4. Criterion 5 ensures the anti-tag condition, which limits the scattering angles of the beam electrons to less than 3.2°. In this thesis, we call this event sample an anti-tag sample. This anti-tag condition ensures the (quasi-) real $\gamma\gamma$ collisions and is important to compare the theoretical predictions consistently. While, the event sample which was selected with the all criteria but the criterion 5 was called a no-tag sample.

The numbers of the events which were selected with the criteria are summarized in the Table 6.1. These selection cuts left 34135 anti-tag events and 43967 no-tag events from the data corresponding to the integrated luminosity of 95.3 and 119.0 pb^{-1}, respectively.

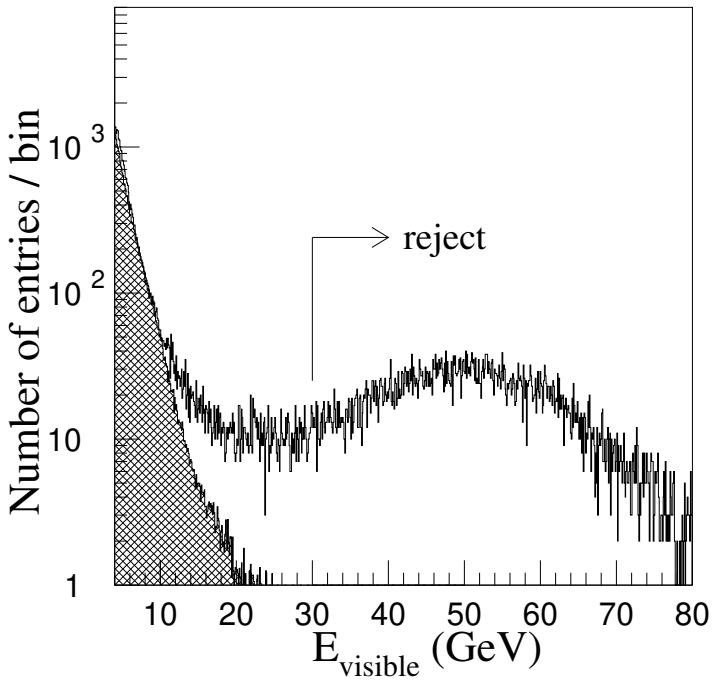

Figure 6.4: $E_{visible}$ distributions for the experimental data (the open histogram) and two-photon events obtained by Monte-Carlo simulation (the hatched one) based on direct + VDM + resolved-photon processes (LAC1).

Selection item		Number of passed events	
		Anti-tag (95.3 pb^{-1})	No-tag (119.0 pb^{-1})
(TOPAZ02 data)	=	4685738	6139177
$\#track \geq 4$	=	342958	365766
$E_{visible} \leq 30$ GeV	=	328210	347562
$W_{visible} \geq 3$ GeV	=	94581	104618
Vertex cut	=	36343	43967
Anti-tagged events	=	34135	-
(Tagged by the BCL)	=	22	-
(Tagged by the ECL)	=	678	-
(Tagged by the FCL)	=	1532	-

Table 6.1: The numbers of the events selected with the criteria.

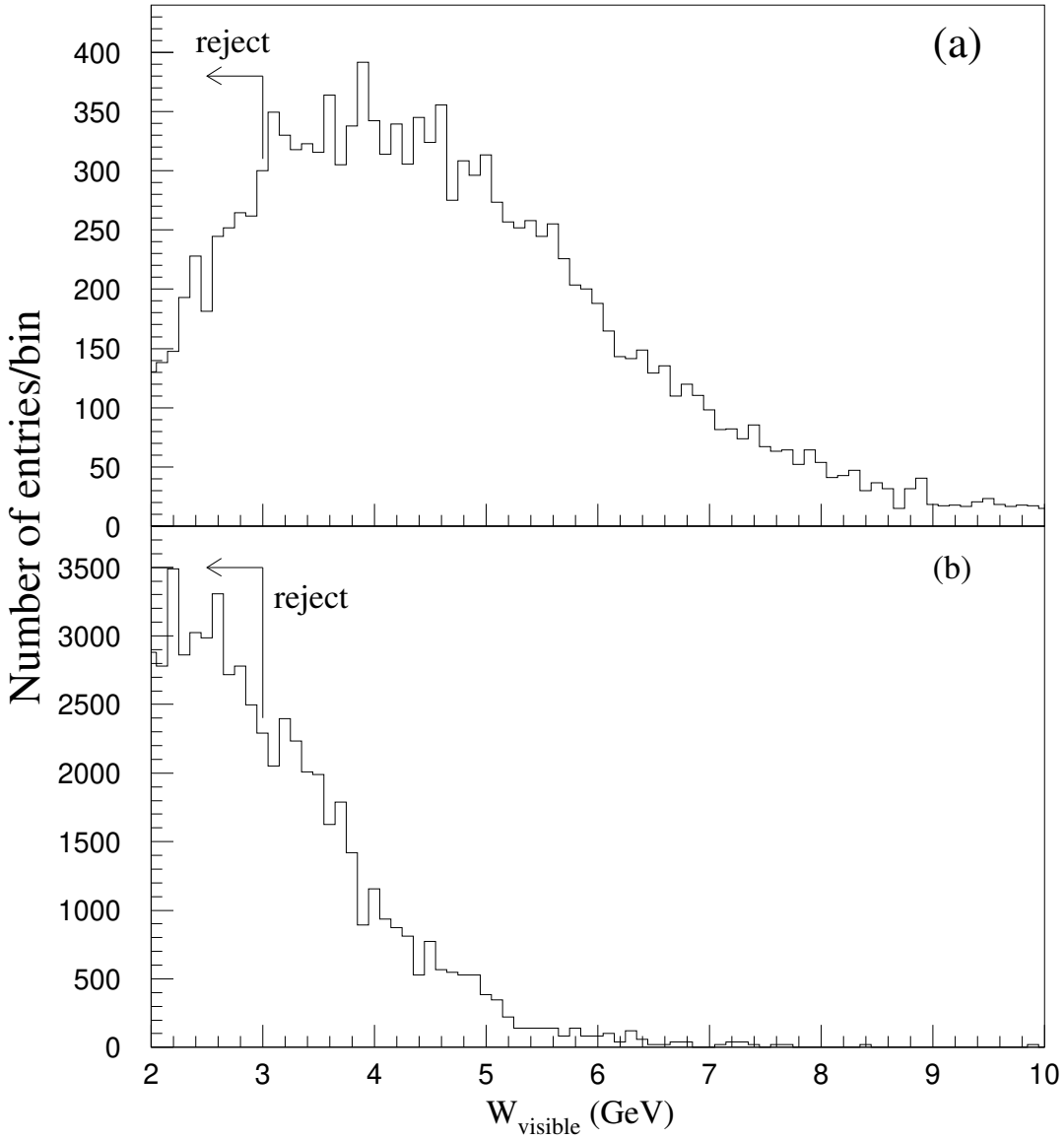

Figure 6.5: W visible distributions for (a) $c\bar{c}$ events and (b) VDM events.

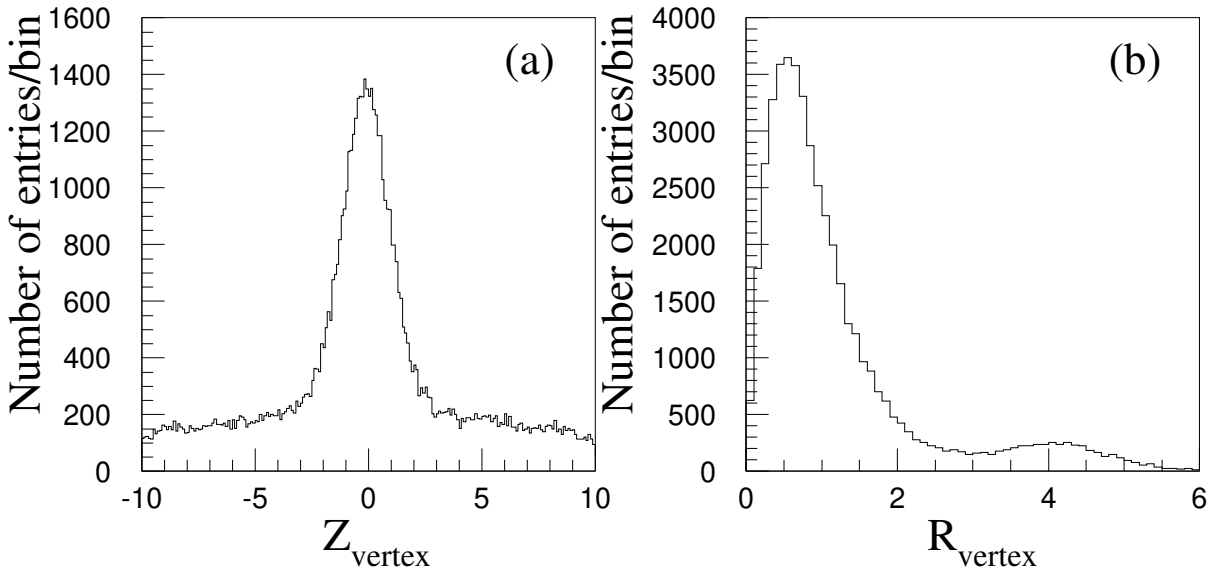

Figure 6.6: Distributions for vertex(a) Z and (b) R.

6.2 Electron identification

Among the selected two-photon events, electron-track candidates were searched. As shown in the Fig. 6.7-(a), the track reconstruction efficiency becomes low at the edge of TPC. Fig. 6.7-(b) show the P_T distribution for the tracks which have the energy deposit in the BCL. In order to ensure good detector performance in the electron identification, we limited the polar angular range and P_T range of the selected electrons to be $|\cos\theta| \leq 0.77$ and $0.4 \leq P_T \leq 3$ GeV.

The TOPAZ detector allows three methods for electron identification. The energy loss (dE/dx) information from the TPC enables us to separate electrons from hadrons in the momentum region $P < 3$GeV[55]. The E/P ratio of the energy(E) measured by the BCL and the momentum(P) measured by the TPC can separate electrons clearly above 1.0 GeV. The TOF was useful to resolve electrons from Kaons and protons in the overlapped region of dE/dx.

6.2.1 Rejection of γ-conversions

Since the largest background source in this analysis was the electrons from the γ-conversions at the material in front of the TPC, we first rejected the dominant

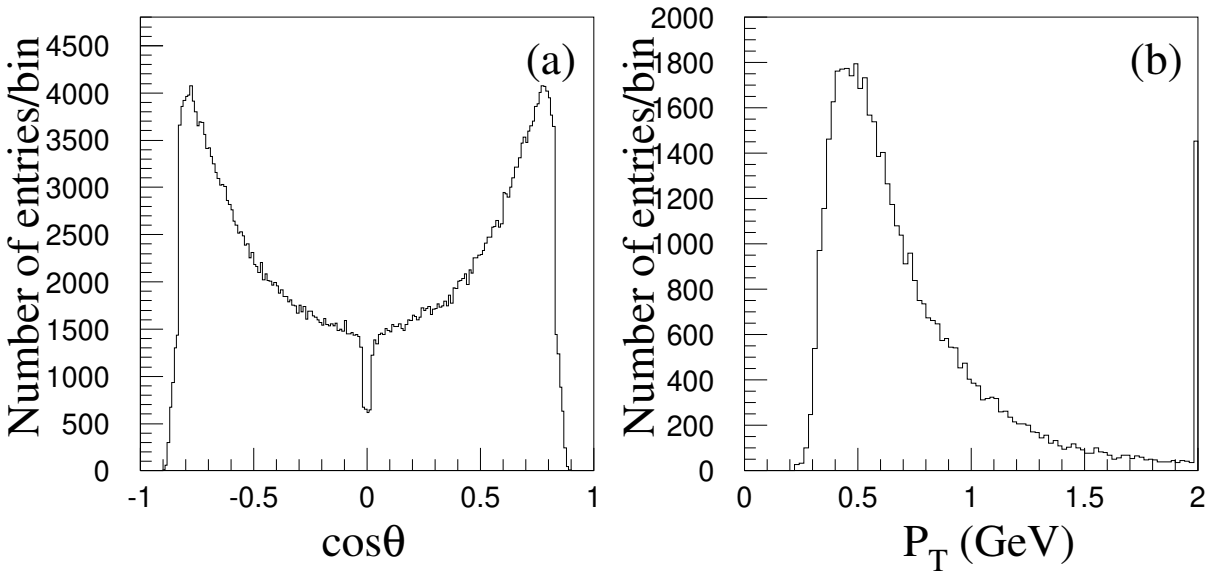

Figure 6.7: Various distributions of (a) $\cos\theta$ for the TPC tracks and (b) P_T for the TPC tracks which have the energy deposit in the BCL.

part of such electrons by the following methods.

We reconstructed secondary vertices of γ-conversion pairs (V^0's) from all combinations of two tracks with opposite charges, and calculated the invariant mass of each V^0 assuming that its daughter particles are electrons. Since the TPC can measure three dimensional positions, we reconstructed V^0's not only in the xy-plane (perpendicular to the beam axis) but also in the z-direction. For the V^0-reconstruction, two kinds of vertices, i.e., non-crossing and crossing cases in the xy-plane were searched, as shown in the Fig. 6.8. In the former case, the distances of the two tracks at the minimum distance position in the xy-plane were required to be less than 7 cm in the xy-plane and 3 cm in the z-direction. In the latter case, we chose from the two crossing points that with the shorter z-difference, and required it to be less than 1.5 cm.

Figs. 6.9 show the various distributions of the V^0's for the γ-conversion pairs in the Monte-Carlo simulation:(a-1) the distance in the xy-plane for the non-crossing case, (b-1) the distance in the z-direction for the non-crossing case, (b-2) that for the crossing case, (c-1) the invariant mass for the non-crossing case, and (c-2) that for the crossing case. The criteria for the V^0-reconstruction were determined with these distributions.

Figs. 6.10 represent the invariant-mass distributions for (a) the non-crossing and (b) the crossing case in the experimental data. We rejected the tracks in the

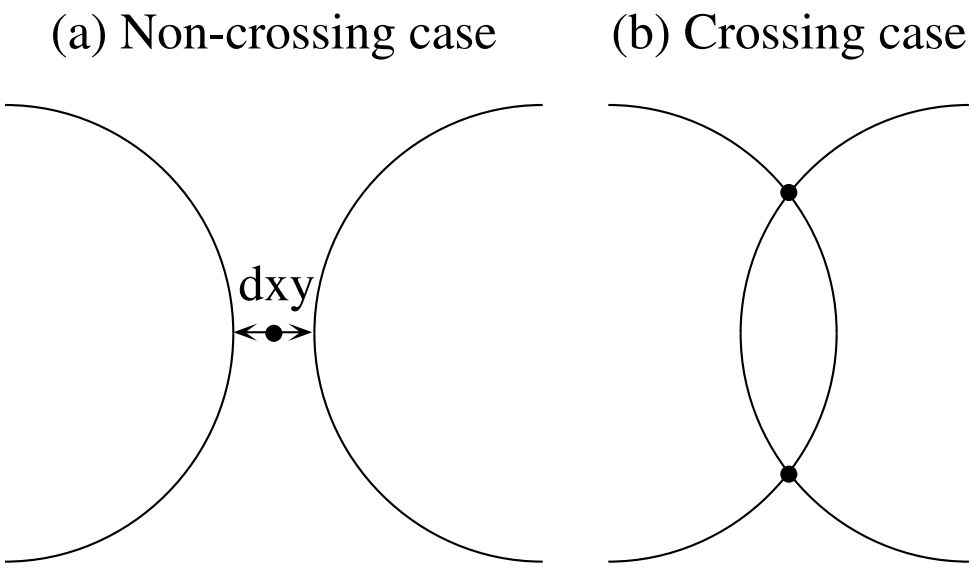

Figure 6.8: Schematic picture for V^0 reconstructions in xy-plane: (a) Non-crossing case and (b) Crossing case.

pair if its invariant mass was $\leq$ 80 MeV in the former or $\leq$ 150 MeV in the latter cases.

We also required the closest approach of each electron-track candidate to the event vertex in the xy-plane to be $<$ 0.5-1.5 cm depending on P_T, as shown in Figs. 6.11.

6.2.2 Electron identification

Among the remaining tracks, electron-track candidates were searched by combining the information of the E/P ratio, the dE/dx, and the TOF as follows:

(1) Charged tracks in the TPC were extrapolated to the BCL. We then selected, for each TPC track, the BCL cluster which was the closest. Figs. 6.12 (a)-1 and -2 show the distributions of the distance between a TPC track and its closest BCL cluster for 1:all tracks and 2:an electron-enhanced sample selected with an dE/dx cut (5.5 $<$ dE/dx $<$ 7.5 KeV/cm) and TOF information. Notice that the dE/dx cut was only used for the purpose of demonstrating the electron identification performance in the figures. We required the electron-candidate tracks to have the TPC-BCL distance of less than 10.0 cm. An energy-weighted r.m.s. of

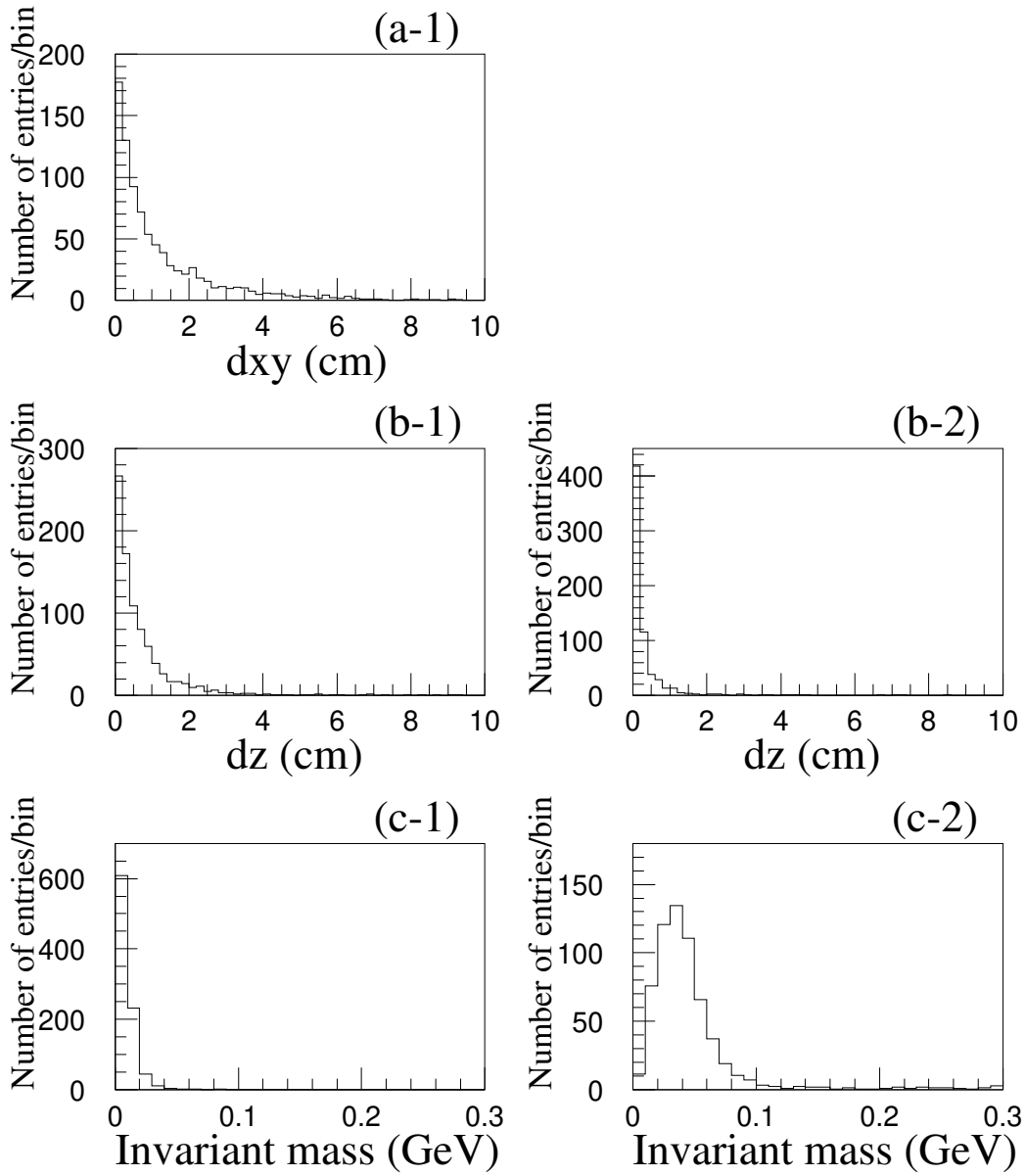

Figure 6.9: Various distributions for the γ-conversion pairs in the Monte-Carlo simulation:(a-1) the distance in the xy-plane for the non-crossing case, (b-1) the distance in the z-direction for the non-crossing case, (b-2) that for the crossing case, (c-1) the invariant mass for the non-crossing case, and (c-2) that for the crossing case.

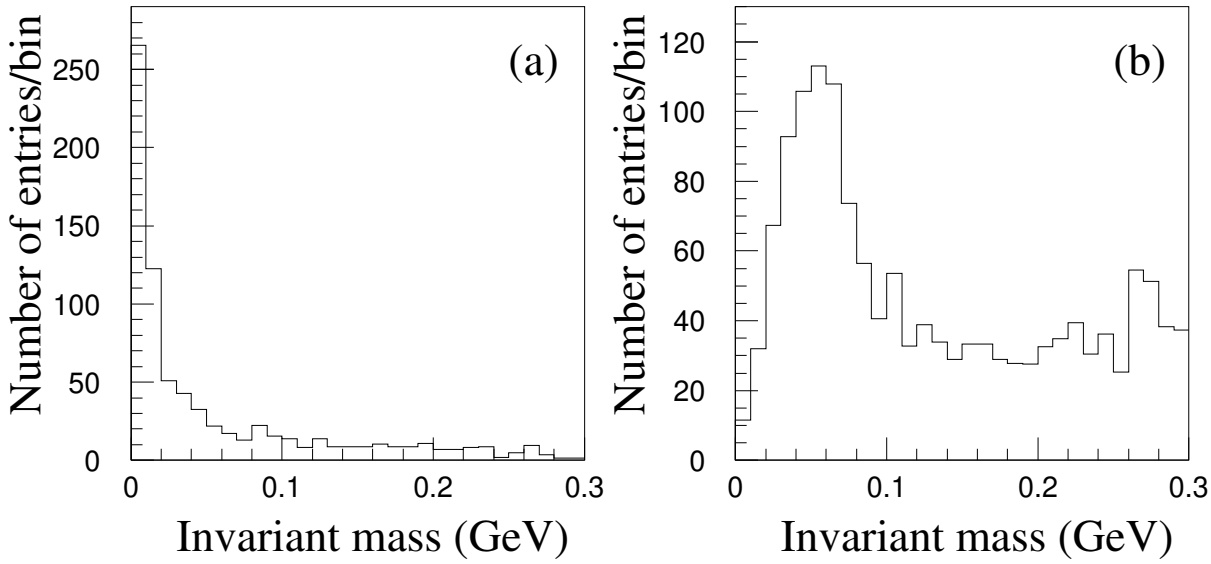

Figure 6.10: Distributions of invariant mass for (a) the non-crossing and (b) the crossing case in the experimental data.

counter positions in the cluster (cluster width) with respect to the extrapolated track position was also calculated. The distribution for the cluster width is shown in Figs. 6.12(b)-1 and -2. Two peaks at 6.0 cm and 8.5 cm ($= \sqrt{6.0^2 + 6.0^2}$ cm) in Fig. 6.12(b)-1 came from the minimum-ionized hadron tracks which were injected into the center of two counters and four counters, respectively. The tracks which have the clusters whose width between 1.0 cm and 10.0 cm were accepted as electron candidates.

We then calculated the E/P ratio of the energy (E) measured by the BCL and the momentum (P) measured by the TPC. The difference between electron-candidate tracks and all charged tracks is shown in Fig. 6.13. The peak at $E/P \sim 1$ corresponds to the electrons. We required the E/P of each of the so-selected TPC-BCL combinations to satisfy $0.75 \leq$ E/P ≤ 1.25. Figs. 6.14 show the E/P distributions at each P_T-bin for the electron candidates selected by dE/dx and the TOF. As shown in the figure, the E/P can identify the electrons effectively at high momentum region($>\sim$1 GeV).

(2) The dE/dx information from the TPC was used as an independent method for electron identification. Figs. 6.15 show distributions for the number of wires used on calculating dE/dx for (a) all tracks and (b) an electron-enhanced sample

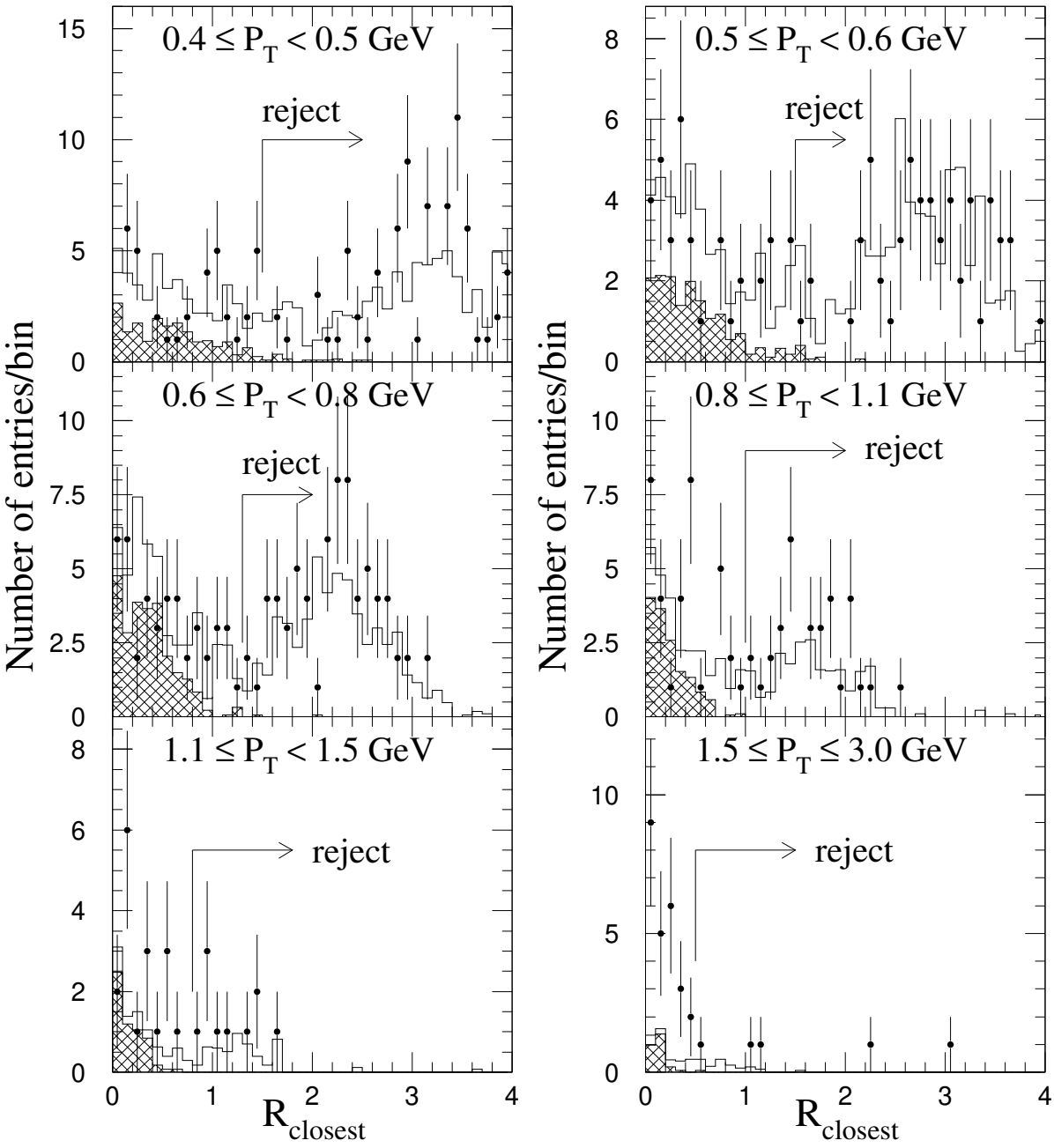

Figure 6.11: Distributions of the closest approach to the event vertex in the xy-plane for each track at each P_T bin. The solid circles are electron candidates in the experimental data. The histograms are electron candidates in Monte-Carlo data (open histograms) and electrons from c-quarks (hatched histograms) obtained by Monte-Carlo simulations.

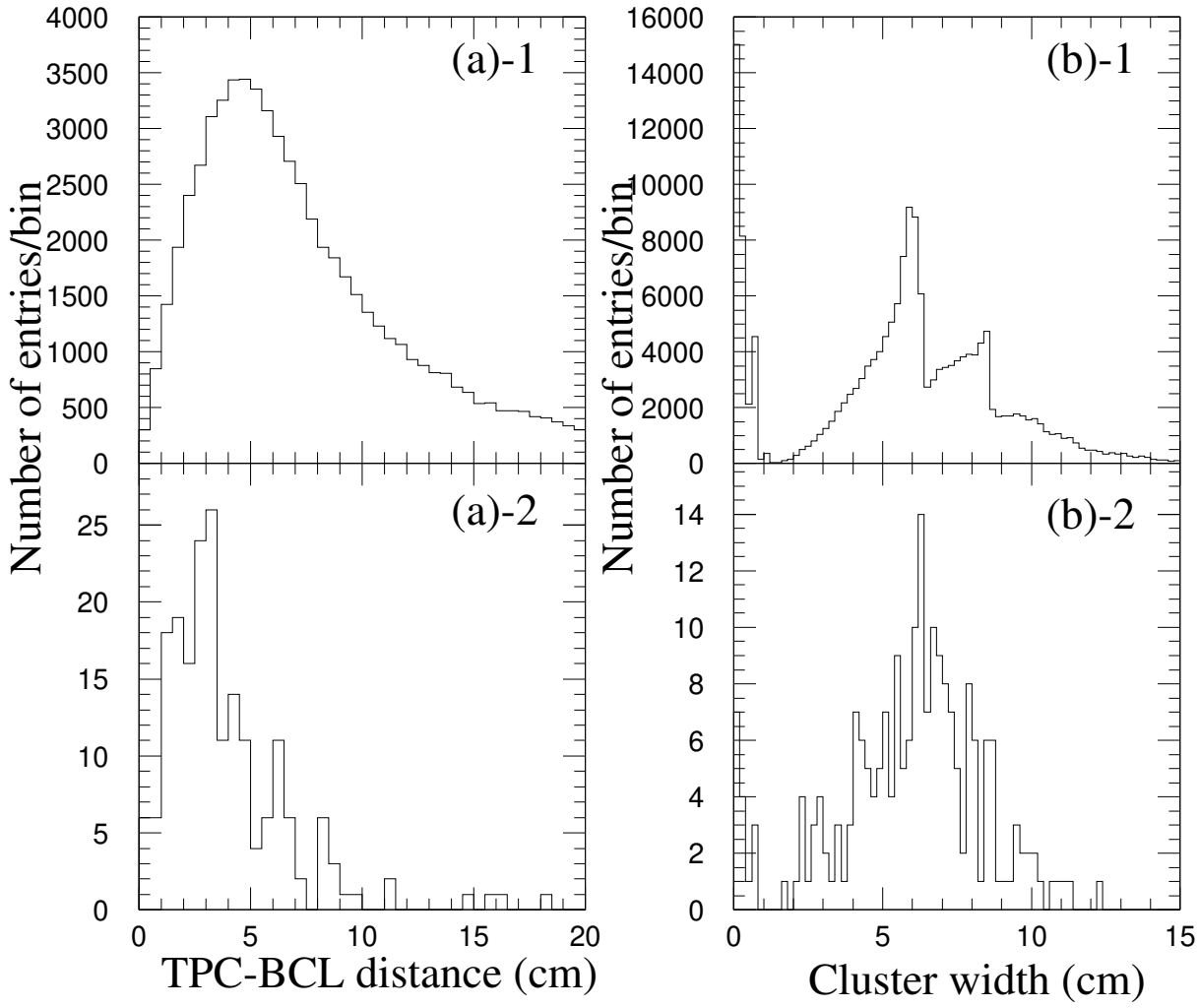

Figure 6.12: Distributions of (a) the closest distance between the TPC track extrapolated point and the BCL cluster and (b) shower width with respect to the track; indices 1 and 2 indicate the all tracks and the electron enhanced samples, respectively.

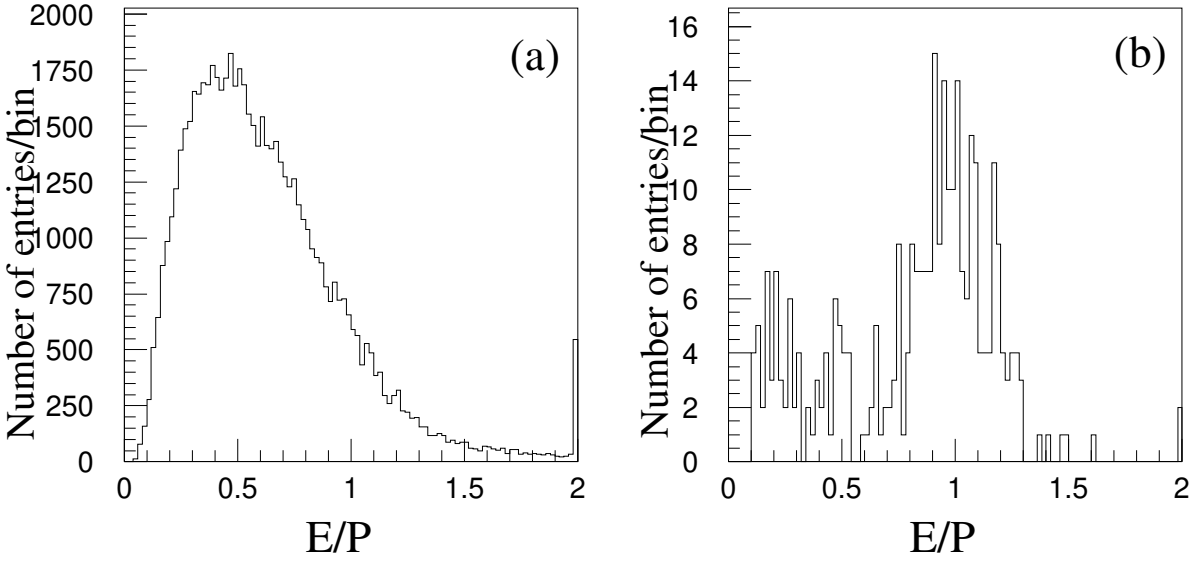

Figure 6.13: E/P distributions for (a) the all tracks and (b) the electron enhanced sample.

selected with the E/P ratio and the TOF. The maximum number of wires 175 was reduced about 110 by the 65% truncated mean method. We used the tracks having the number of used wires for calculating the dE/dx of lager than 75. The resultant dE/dx was mostly contained in the range $5.5 \leq dE/dx \leq 7.5$ keV/cm. As can be seen from the dE/dX distributions in Fig. 6.16-(b), two peaks corresponding to electrons and pions are clearly separated.

Figs. 6.17 show the dE/dx distributions at each P_T bin for electron candidates selected by the E/P ratio and the TOF. At all P_T bins, electrons and pions are clearly separated. The dE/dx information is crucial to identify the low-P_T electrons which could not done by the E/P alone.

(3) Finally, we used information from the TOF and required the track to have a confidence level(CL) of 0.01 or better for the electron hypothesis. Fig. 6.18 shows distribution of the CL for the electron hypothesis in the TOF for an electron-enhanced sample which was selected with E/P ratio and the dE/dx cut ($5.5 <$ dE/dx < 7.5 KeV/cm). As described above, the dE/dx cut was only used for the purpose of demonstration. Figs. 6.19 show the dE/dx distributions for the tracks which were identified with the E/P ratio but the TOF (open area) and for the tracks which were rejected with the TOF (hatched area) at each P_T bin. As shown in the figures, the TOF information was effective to remove Kaons and protons in the dE/dx overlap region.

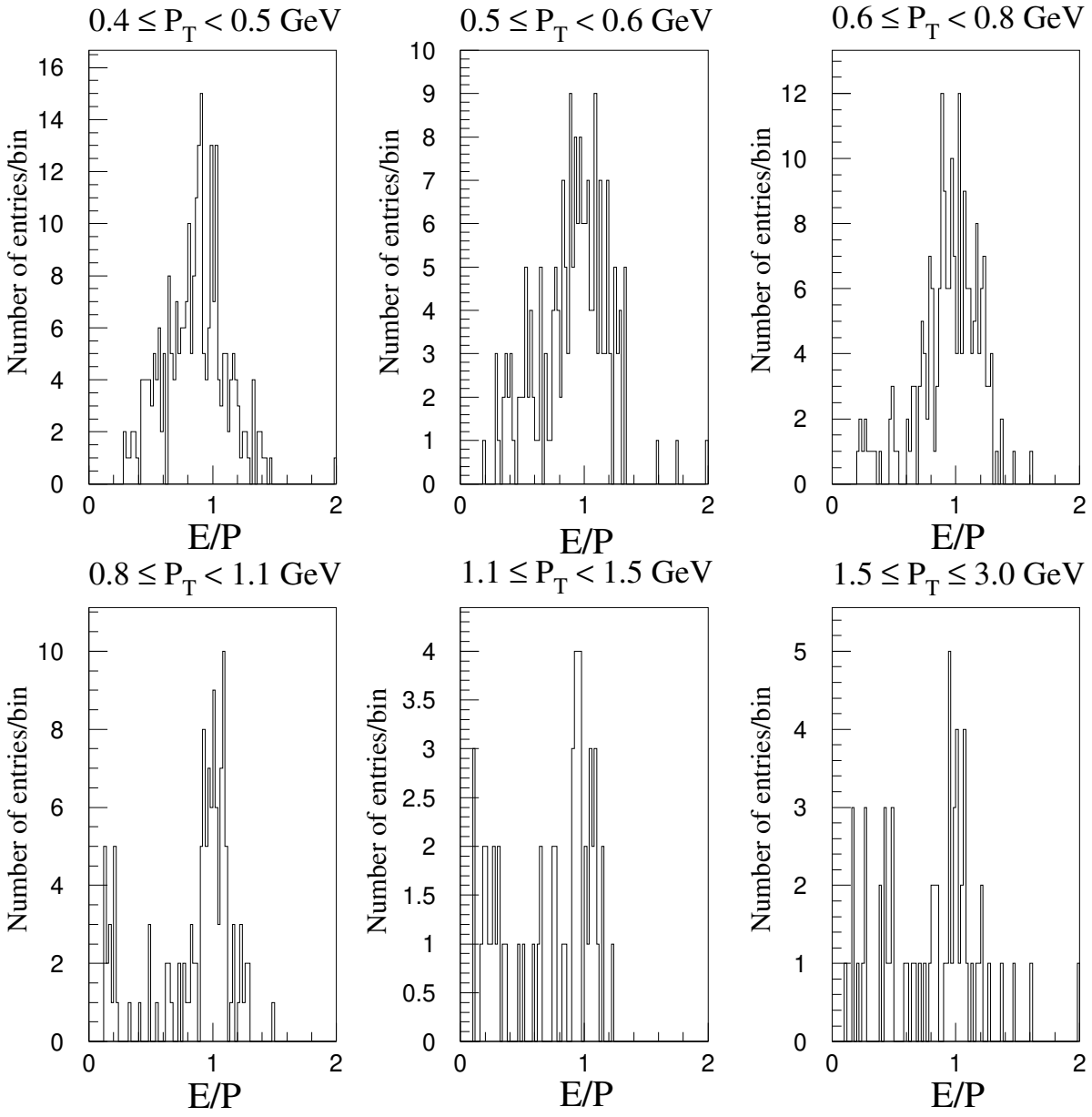

Figure 6.14: E/P distributions at each P_T bin.

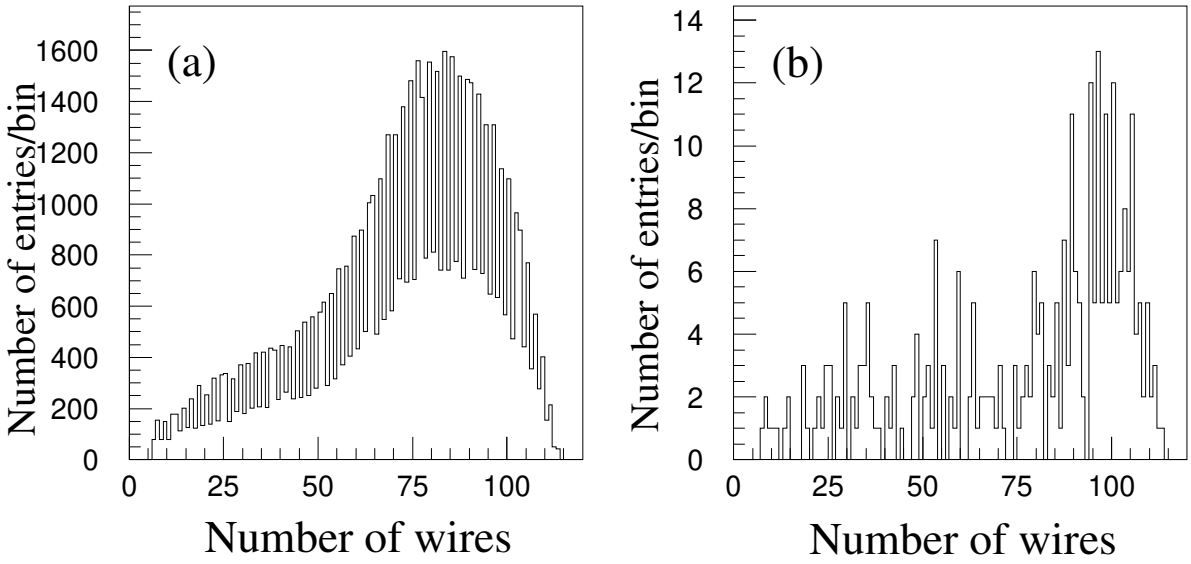

Figure 6.15: Distributions for the number of wires used on calculating dE/dx for (a) the all tracks and (b) the electron enhanced sample.

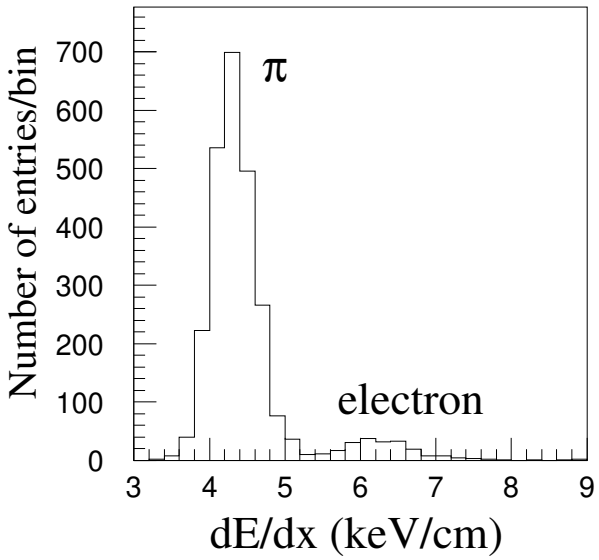

Figure 6.16: Distribution of the dE/dx for electron candidate tracks. Where electrons and pions are clearly separated.

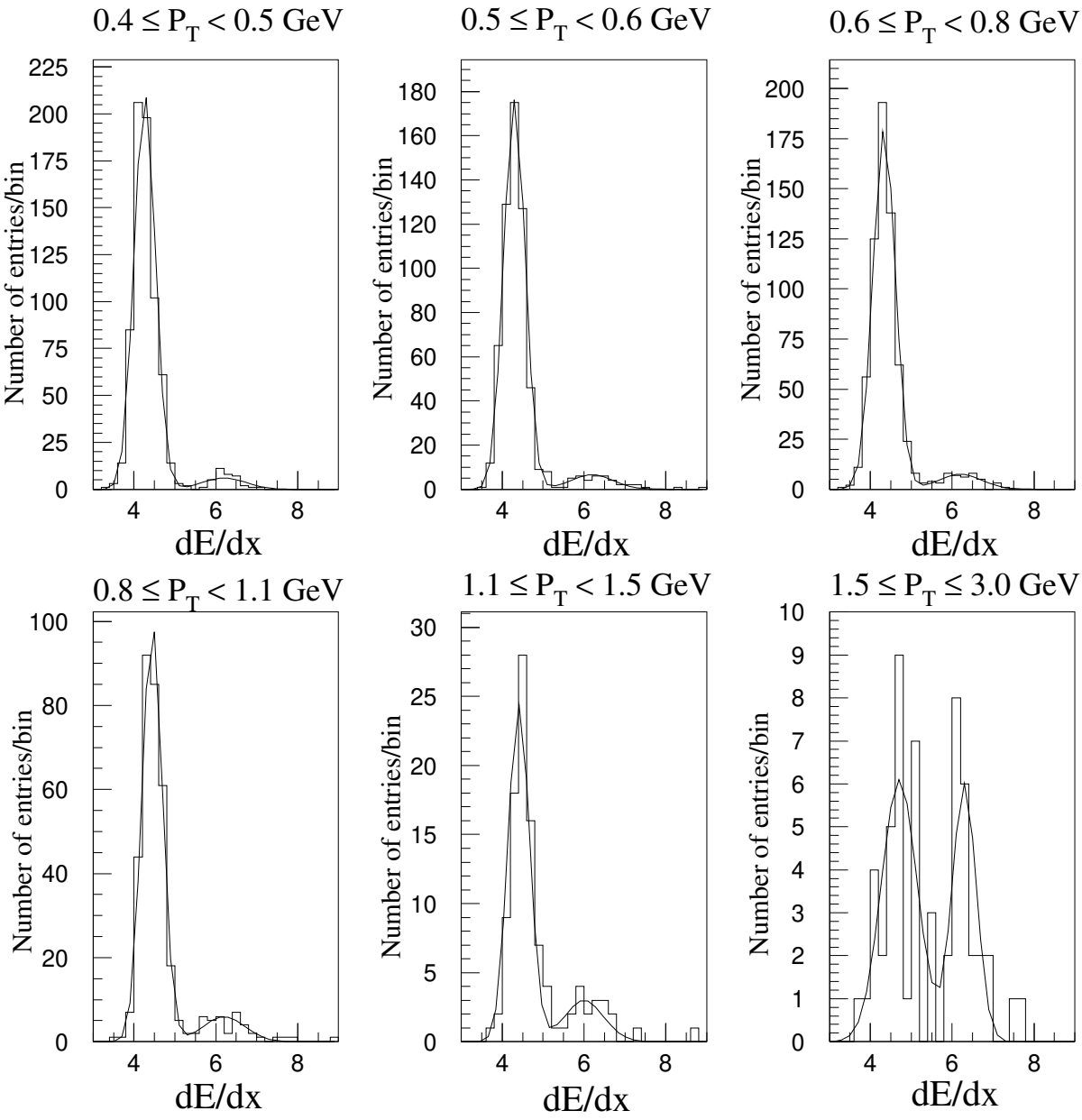

Figure 6.17: Distributions of dE/dx for electron candidates at each P_T bin. The solid lines are fitting lines described in the text.

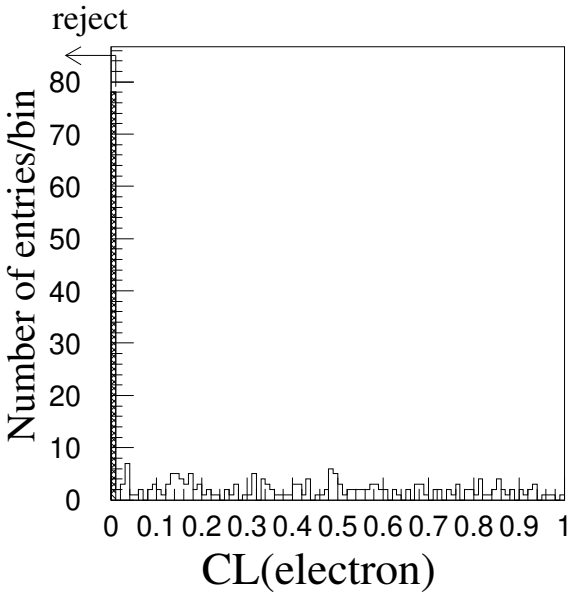

Figure 6.18: Distribution of the CL for the electron hypothesis in the TOF.

We counted the numbers of electrons in each P_T bin by fitting the dE/dx distributions with double Gaussians bin by bin. The P_T binning was selected so as to approximately equalize the number of entries in each bin. The P_T resolutions were smaller than the bin width. The numbers obtained are plotted (solid circles) in Fig. 6.24. The errors are statistical. The numbers of electron candidates summed over the P_T bins were 214.8 ± 15.4.

6.2.3 Electron selection efficiency

Electron selection efficiency was derived using single-track and multi-hadron events generated by the Monte-Carlo simulations. All of the tracks identified by the above electron-selection procedure were counted. The definition of the selection efficiency is the ratio of the number of electrons counted (as above) to the number of electrons before the electron selection criteria was applied. The electron efficiencies for single-track events and for multi-hadron events are shown in Figs. 6.20 and 6.21, respectively, as a function of the transverse momentum of the track. The average values of the efficiencies were $34.2 \pm 1.0\%$ for single-track events and $36.0 \pm 0.8\%$ for multi-hadron events. The former value was obtained assuming the P_T distribution in the multi-hadron events.

The pion-rejection factors were also derived with single-track and multi-hadron events. For single-track events we obtained a pion-rejection factor of 15000 for the

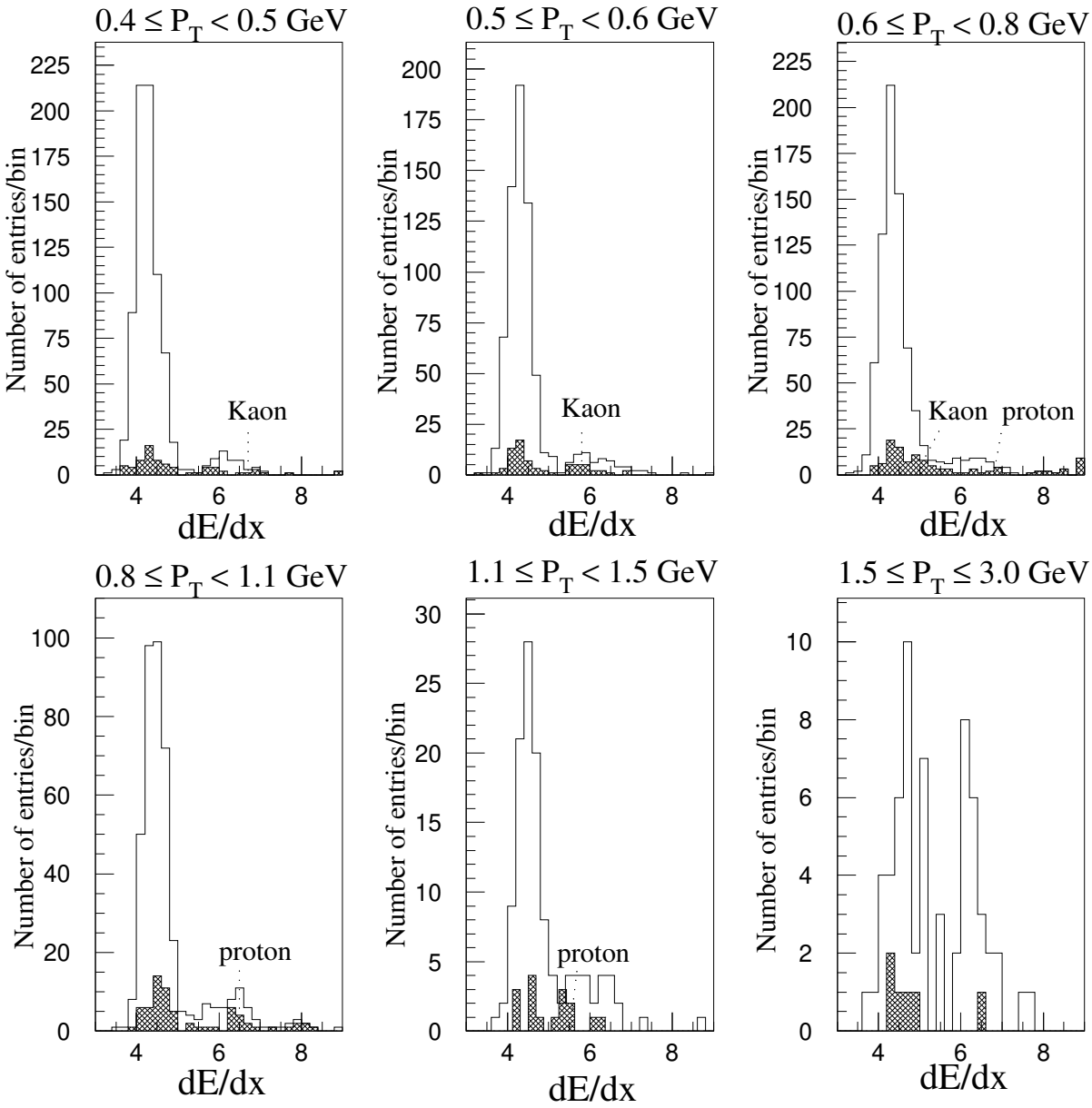

Figure 6.19: Distributions of dE/dx for the electron candidates selected without the TOF cut (open histograms) and that for the tracks which are rejected with the TOF (hatched histograms). The hadrons in the dE/dx overlap regions are rejected.

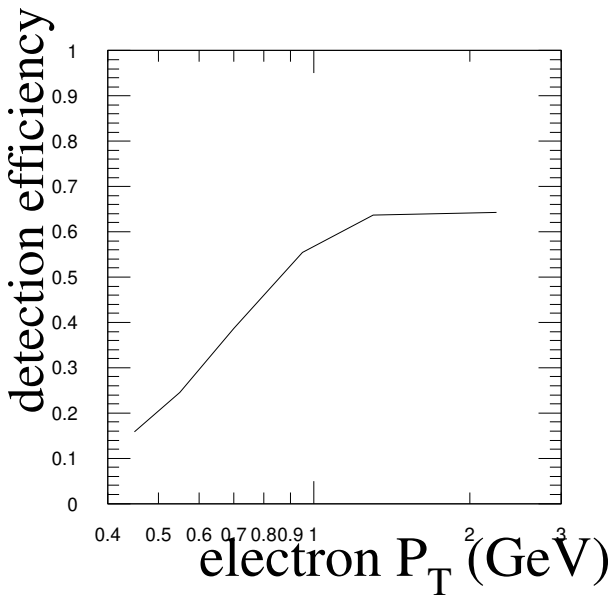

Figure 6.20: Detection efficiency of electron tracks for single-track events.

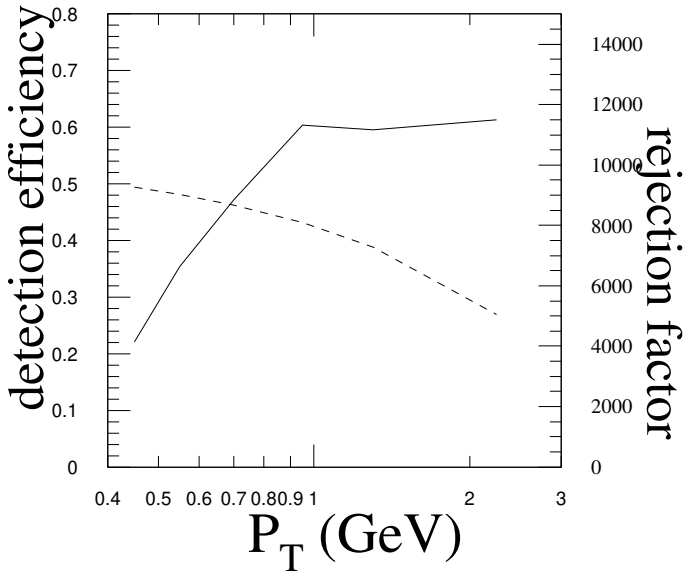

Figure 6.21: Pion-rejection factor and electron efficiency for two-photon hadronic events; the dashed curve is the pion-rejection factor (right scale) and the solid one is the electron efficiency (left scale).

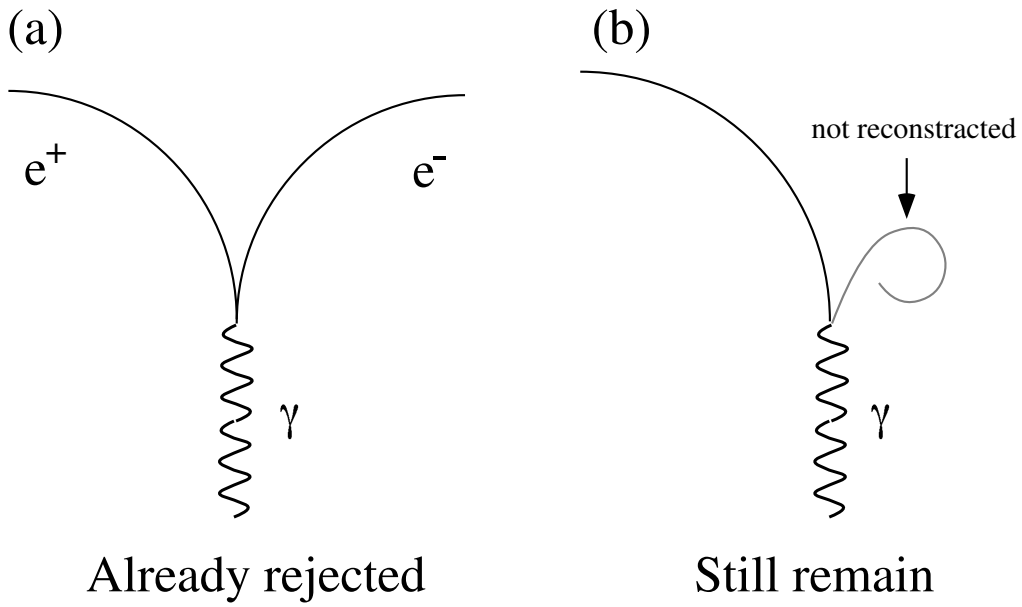

Figure 6.22: Schematic picture for the γ-conversions.

high momentum region of $1.5 \leq P_T \leq 3.0$ GeV where the factor was the smallest. The pion-rejection factor for multi-hadron events is indicated in Fig. 6.21 by the dashed line. The average value for multi-hadron events was 8600. In the present analysis we counted the number of electrons by fitting the dE/dx distributions. Therefore, in fact, the pion-rejection factor was far better than these values.

6.3 Background estimation

These electron candidates include background tracks coming from sources other than charm-quark decays. These background sources were studied in detail.

There remained electrons coming from γ-conversions which escaped from pair reconstruction. They were presumably energy-unbalanced pairs, for each of which the lower P_T track was not reconstructed by the TPC as shown in Fig. 6.22. We estimated the failure rate of the V^0 reconstruction by a Monte-Carlo simulation. The failure rate,

$$\eta = \frac{N^{M.C.}_{V^0 failure}}{N^{M.C.}_{V^0 reconstructed}}, \tag{6.1}$$

was estimated for each P_T-bin and was typically $\sim$0.4 as shown in Fig. 6.3. In the calculation, we included contributions from Dalitz decay($\pi^0 \rightarrow e^+e^-\gamma$) as well as the conversion electron pairs. In order to estimate the number of remaining back-

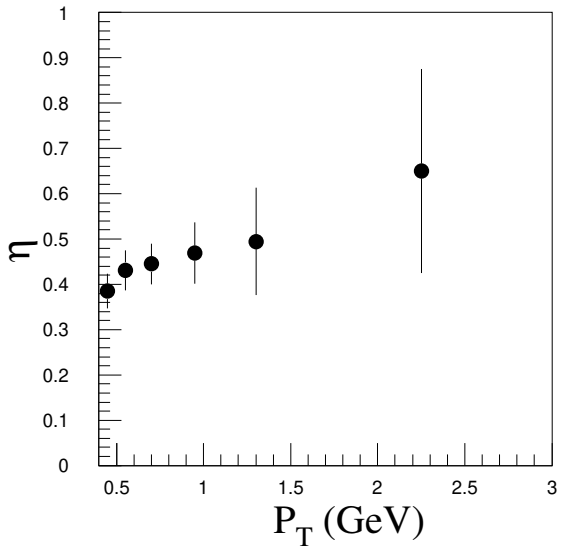

Figure 6.23: The failure rate of the V^0 reconstruction as a function of P_T estimated by a Monte-Carlo simulation.

ground tracks from γ-conversions, we multiplied the number of the reconstructed conversion pairs in the experiment by η in each P_T bin;

$$N^{exp}_{V^0 remained} = \eta \cdot N^{exp}_{V^0 reconstructed}, \tag{6.2}$$

and obtained the cross-hatched histogram in Fig. 6.24. With this method, we can estimate the remaining γ-conversions independently of the π^0 multiplicity at generator level. The γ-conversion and Dalitz decay background mainly occupy the low-P_T region, and comprise 23.8% of the selected electron sample.

The background from the single-photon annihilation ($e^+e^- \to (\gamma) \to q\bar{q}$) was estimated by a Monte-Carlo simulation with JETSET 6.3[50]. The parameters of this Monte-Carlo program have been tuned by fitting the TOPAZ single-photon annihilation data[56]. We set the maximum fractional photon energy (k_{max}) to be 0.99 for initial-state radiation. The result is shown in Fig. 6.24 by the open area of the histogram. The electrons which came from single-photon annihilations had high P_T in general, and were estimated to be 11.8%.

The contributions from the $e^+e^- \to e^+e^-\tau^+\tau^-$ and $e^+e^- \to \tau^+\tau^-$ processes were studied by Monte-Carlo simulations which were used in previous four-lepton[28, 57] and lepton pair production[58] analyses. The result is shown in Fig. 6.24 as the

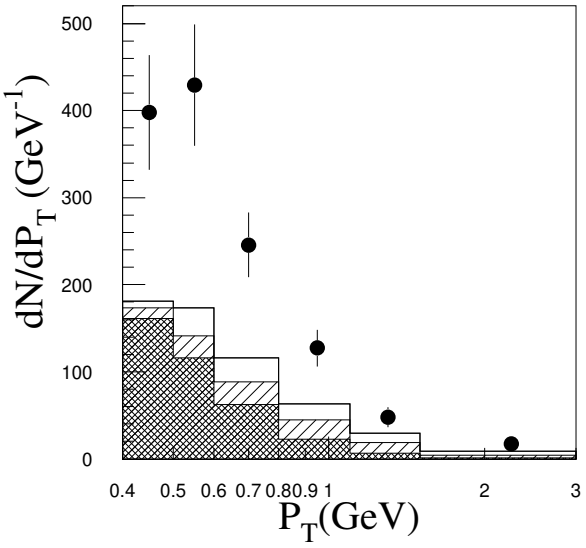

Figure 6.24: Observed number of electrons as a function of P_T. The solid circles are the experimental data. The histograms are the background components: γ-conversions and π^0 Dalitz decays (cross-hatched area), $e^+e^- \rightarrow e^+e^-\tau^+\tau^-$ (the singly-hatched area), and single photon annihilations (the open area).

singly-hatched area of the histogram, which corresponds to 12.1% of the selected electron sample. This background has a broad P_T distribution.

As for the $e^+e^- \rightarrow e^+e^-e^+e^-(\gamma)$ process, we checked its contamination experimentally. First, we searched for events consisting of tracks all of which were consistent with the electron hypothesis (using dE/dx). The contamination was only 3.0%. The change of the cut on the charged multiplicity in the event selection from 4 to 5 made only 1.6% difference seen in the electron yield. We took these numbers as being systematic errors in the cross-section evaluation.

The beam-gas background was checked by using off-vertex events. The electron yield in these events was consistent with zero.

These background contributions were subtracted from the data on a bin-by-bin basis in further analysis. In total, 112.3 $\pm$ 15.4(stat.) $\pm$ 11.9(sys.) electrons remained after the background subtraction.

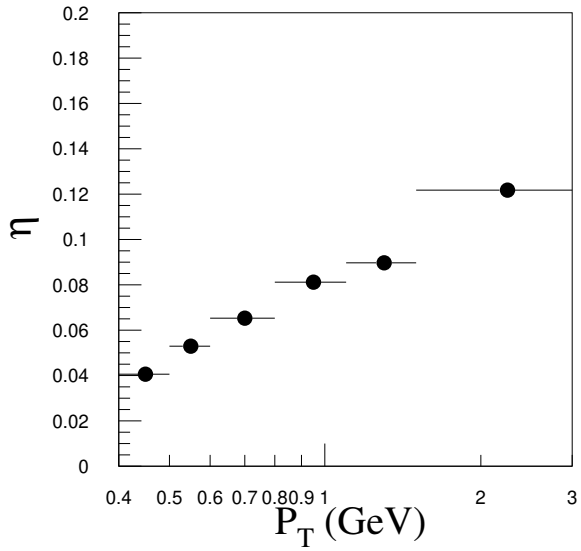

Figure 6.25: Acceptance (η) as a function of the P_T.

6.4 Inclusive-electron cross section

6.4.1 Acceptance correction

In order to compare the data with the theoretical predictions directly, we carried out acceptance corrections and measured the transverse momentum(P_T) dependence of the inclusive electron cross sections in $\gamma\gamma$ collisions:

$$e^+e^- \rightarrow (e^+e^-) + e^{\pm} + X,$$

with the anti-tag condition of $\theta_{max} \leq 3.2°$. As mentioned earlier, the polar angles of the selected electrons were limited to $|\cos\theta| \leq 0.77$ in order to ensure good detector performance in the electron identification. The acceptance includes the detection efficiency of the hadronic two-photon event and the electron-selection efficiency.

The overall acceptance was determined by the Monte-Carlo simulations of the direct and resolved processes. The resultant acceptance increases smoothly from 5% to 12% as the electron-P_T goes up from 0.4 GeV to 3.0 GeV (shown in Fig. 6.25).

P_T range (GeV)	0.4 - 0.5	0.5 - 0.6	0.6 - 0.8	0.8 - 1.1	1.1 - 1.5	1.5 - 3.0
ee $\rightarrow$ ee $\tau\tau$	1.6	2.1	2.8	4.3	8.9	5.6
ee $\rightarrow$ hadron	1.7	3.2	3.9	5.2	11.2	8.3
γ-conv. (V^0 statistic)	11.8	10.9	10.6	12.4	18.3	11.3
γ-conv. (η statistic)	6.6	4.9	4.6	5.0	7.5	4.1
γ-conv. (η systematic)	0.8	5.2	12.6	3.2	7.5	4.1
ee $\rightarrow$ eeee	2.4	0.7	4.1	2.3	41.1	23.5
cut dependence	17.4	13.8	13.1	11.9	26.8	11.4
dE/dx fitting	6.4	8.9	3.0	2.6	1.1	13.8
acceptance correction	4.3	4.3	3.8	5.0	7.9	9.2
Total	23.6	21.8	23.0	20.3	55.9	34.7

Table 6.2: Systematic errors. (Percentage (%) to final inclusive-electron cross section in each P_T binning.)

6.4.2 Systematic errors

The systematic uncertainty for the measurement of the inclusive-electron cross section came from the various sources summarized in Table 6.2. We discuss the each item below.

1. The uncertainty from the background estimation for γ-conversions and Dalitz decays was estimated to be 10 - 18% by changing the cuts on V^0 reconstruction, and by using independent information from the inner tracking device. Since we used the actual number of V^0's to estimate the background, the statistical error on that number was dominant.

2. The cut dependence was studied by changing the cuts for the event and electron selections by $\pm$10% from the nominal cut values. The uncertainty estimated by this way was about 15%.

3. Two fitting methods were applied in order to obtain the number of electrons from the dE/dx distribution in each P_T bin. First, the fitting was carried out by fixing the center value and the resolution to the values obtained from the entire electron sample. In the second method, the fitting was carried out by making these parameters completely free. The two methods gave a difference of about 5%.

4. The uncertainty in the luminosity measurement was 4%.

electron-P_T	$d\sigma/dP_T$	
(GeV)	anti-tag	no-tag
0.4 - 0.5	56.4 ± 17.5 ± 13.3	65.7 ± 16.0 ± 15.0
0.5 - 0.6	47.1 ± 12.5 ± 10.3	44.9 ± 11.1 ± 9.8
0.6 - 0.8	20.9 ± 6.2 ± 4.8	25.5 ± 5.5 ± 5.6
0.8 - 1.1	8.1 ± 2.6 ± 1.7	12.0 ± 2.7 ± 2.1
1.1 - 1.5	2.4 ± 1.3 ± 1.3	3.7 ± 1.3 ± 2.0
1.5 - 3.0	0.8 ± 0.3 ± 0.3	0.9 ± 0.3 ± 0.3

Table 6.3: Differential cross sections $d\sigma/dP_T$ ($|\cos\theta| \leq 0.77$)(pb/GeV) of inclusive electron productions shown as functions of the electron-P_T. The cross sections with anti-tag and no-tag conditions are shown in the table, where the cross section under the no-tag condition was obtained from the sample without the anti-tag cut (criterion 5) in section 6.1. This cross section was obtained by using the detection efficiency calculated with the photon-flux factor of eq. 2.21 with $\theta_{max} = \pi$.

5. The Monte-Carlo statistics for the acceptance correction and the background estimation for the processes $e^+e^- \to e^+e^-\tau^+\tau^-$ and $e^+e^- \to q\bar{q}$ were treated as systematics errors. The total systematic error from the Monte-Carlo statistics was 5%.

6. As described earlier, we regarded the $e^+e^- \to e^+e^-e^+e^-$ background as being a systematic error source. The systematic error from this source differed from bin to bin, but was typically about 4%.

The total systematic errors were obtained to be from 20 to 35%, depending on the value of P_T.

6.4.3 Result

The measured inclusive-electron cross section as a function of the electron P_T ($|\cos\theta| \leq 0.77$) is shown in Table 6.3 as well as in Fig. 6.26. In the table, the first errors are statistical and the second ones are systematic. The errors in the figure include both of these errors added in quadrature.

The inclusive-electron cross section integrated over the intervals $0.4 \leq P_T \leq 3.0$ GeV and $|\cos\theta| \leq 0.77$ was measured to be

$$19.3 \pm 2.7 \text{ (stat.)} \pm 2.1 \text{ (sys.) pb.}$$

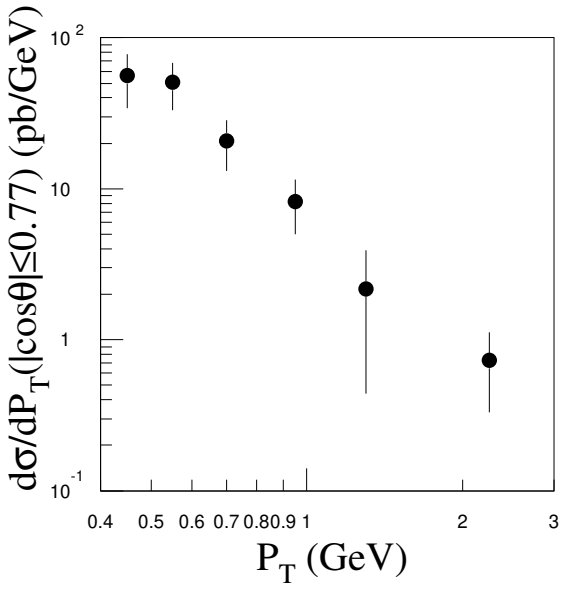

Figure 6.26: Differential cross section of inclusive electrons as a function of the electron-P_T, imposing the anti-tag condition.

Chapter 7

Remnant-jet analysis

7.1 Remnant-jet tagging

As described in Chapter 1, the remnant-jets are expected to be produced in the small-angle region in the resolved-photon processes. Since remnant-jets do not exist in the direct process, this is the direct evidence of the resolved-photon. Fig. 7.1 represents the energy distributions for anti-tagged events. As shown in the figure, substantial part of the anti-tagged events have some activities, though of relatively low energy, in the FCL. Our Monte-Calro study showed that these activities can be naturally understood by remnant jets which are produced predominantly to the beam direction in the resolved-photon processes[10, 59] (shown in Fig.7.2). For more detailed study of these events, we selected them by adding the following criterion to the anti-tag event selection cuts described in section 6.2.2:

- The energy deposit in the FCL has to be 0.5 GeV $< E_{vis}^{FCL} < 0.25 E_{beam}$.

They are called remnant-jet-tagged events. The selection cuts left 16646 remnant-jet-tagged events from 34135 anti-tagged events (48.8%).

With the Monte-Carlo simulation of the resolved-photon process, the efficiency of the remnant-jets leaving an activity greater than 0.5 GeV in the FCL was evaluated to be 73$\pm$2%, where the error was obtained by comparing the two cases both with and without an intrinsic P_T ($\sim$ 0.4 GeV) in the remnant-jet production. On the other hand, that of the direct process was estimated to be small (about 7%). This contribution was subtracted in order to obtain the cross section of the resolved-photon process.

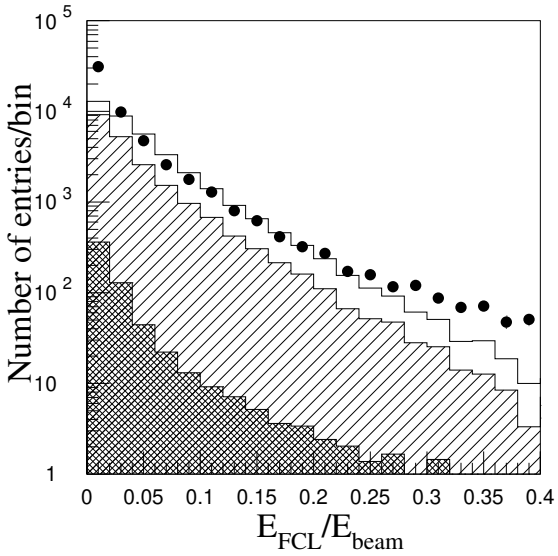

Figure 7.1: Distribution for the energy deposit in the FCL. The solid circles are the experimental data. The histograms are Monte-Carlo data based on the direct only (the double hatched histogram), direct + VDM (the single hatched histogram), and direct + VDM + LAC1 (the open histogram).

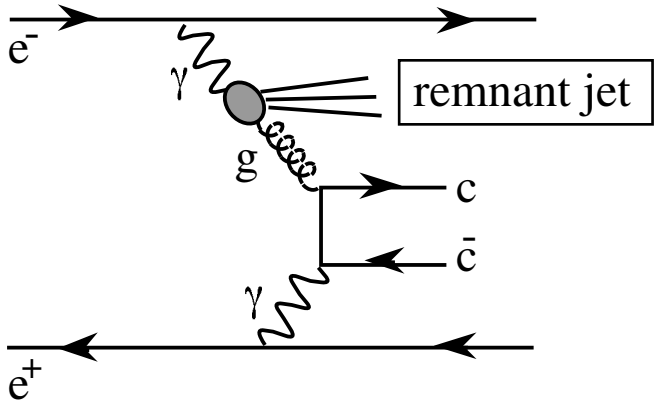

Figure 7.2: Feynman diagram for the 1-resolved photon process which contributes the open-charm production. The remnant jet is produced in the beam direction.

7.2 Electron identification

Among the selected remnant-jet-tagged events, we searched the electron-candidate tracks with the same procedure as described above. Using the dE/dx distributions at each P_T bin, we counted the number of the electrons, as shown in the Fig. 7.3. In the figure, the electrons from γ-conversions were already rejected with V^0 reconstruction described in Section 6.2.1. Since the statistics is less than that of in the anti-tag analysis, we used the same center value determined in the anti-tagged analysis for the electron dE/dx. The numbers of electron candidates summed over the P_T bins were 88.0 ± 9.3 for the remnant-jet-tagged sample.

7.3 Background estimation

We then estimated the background tracks coming from the following sources:

- remaining γ-conversions 27.8%,
- $e^+e^- \rightarrow e^+e^-\tau^+\tau^-$, $e^+e^- \rightarrow \tau^+\tau^-$ 3.6%,
- e^+e^- →hadrons 13.2%,
- contamination from direct process 6.6%.

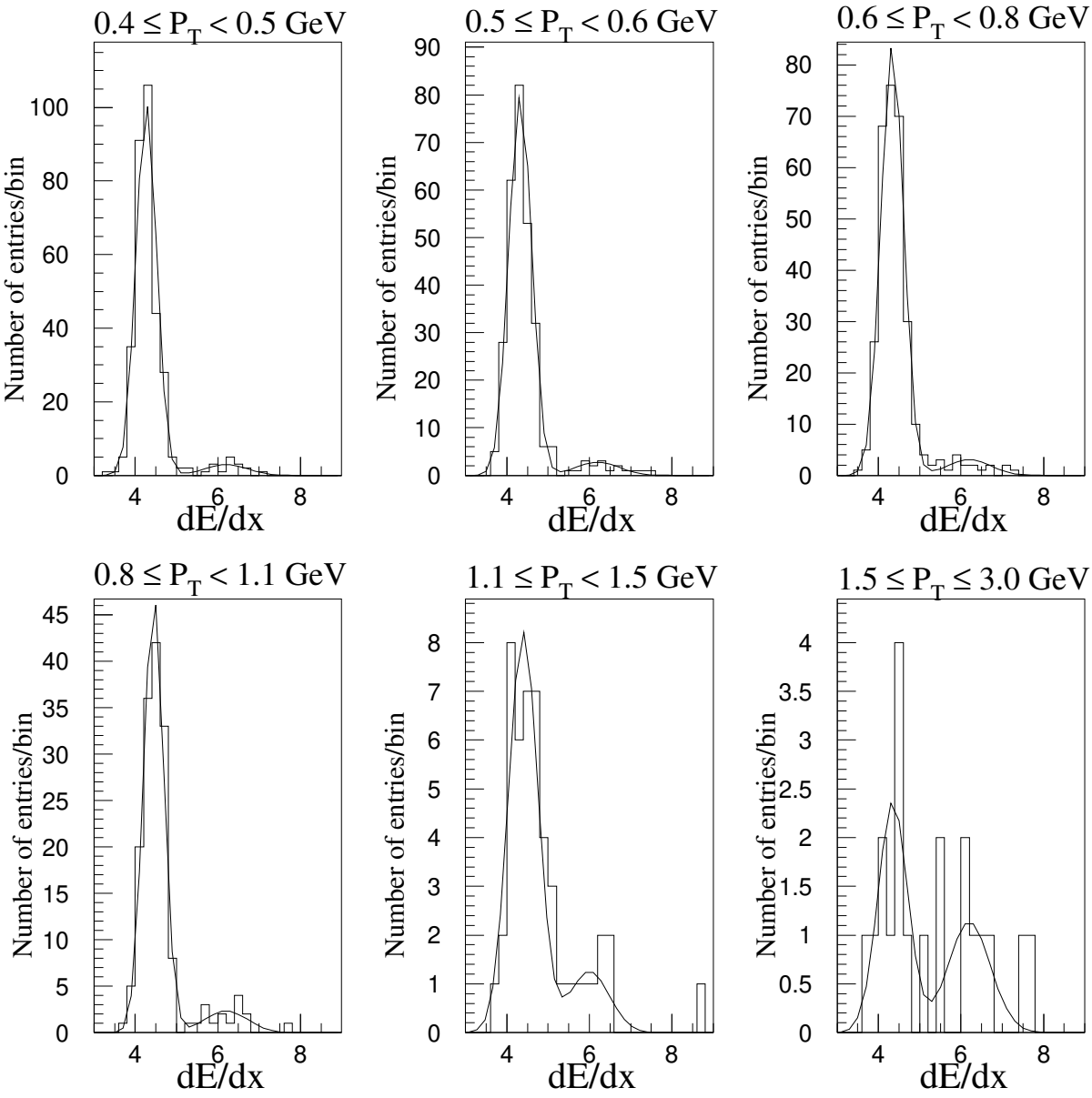

Figure 7.3: Distribution of dE/dx for electron candidates in the remnant-jet-tagged sample. The fitting method is described in the text.

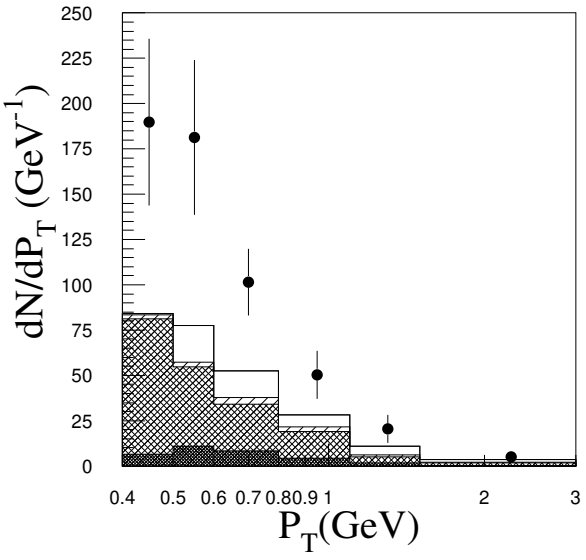

Figure 7.4: Observed number of electrons as a function of P_T. The solid circles are the experimental data. The histograms are the background components: the direct process events (the filled area), γ-conversions and π^0 Dalitz decays (the cross-hatched area), $e^+e^- \rightarrow e^+e^-\tau^+\tau^-$ (the singly-hatched area), and single photon annihilations (the open area).

In spite of an extensive shielding system protecting the FCL from beam-induced background, continuous(random) activities were still observable. These activities were estimated to be 10% from independent event samples (large-angle Bhabha events and random triggered events) and were subtracted. These background contaminations are shown in Fig. 7.4.

In total, 42.9 $\pm$ 9.3(stat.) $\pm$ 6.2(sys.)(remnant-jet-tag) electrons remained after the background subtraction.

7.4 Inclusive-electron cross section

7.4.1 Acceptance correction

In order to obtain the cross section for resolved-photon process, the acceptance was determined by the Monte-Carlo simulation of a resolved-photon processes where LAC1 was used for the parton density in the photon. The resultant acceptance as the electron-P_T is shown in Fig. 7.5.

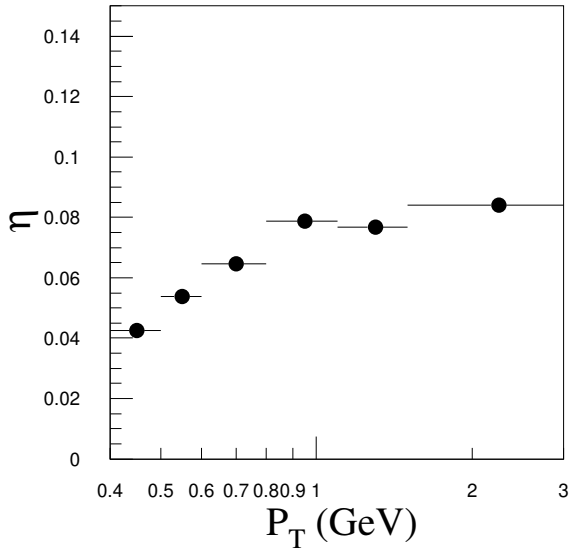

Figure 7.5: Acceptance (η) as a function of the P_T.

7.4.2 Systematic errors

We estimate the following systematic uncertainty with the same method as described in the previous section:

1. The uncertainty from the γ-conversion background estimation;
2. The selection cut dependence;
3. The dE/dx fitting uncertainty;
4. The Monte-Carlo statistics for the acceptance correction and background estimation of the $e^+e^- \to e^+e^-\tau^+\tau^-$, e^+e^- →hadron, and the direct process;
5. The contamination for $e^+e^- \to e^+e^-e^+e^-$; and
6. The uncertainty in the tagging efficiency of the remnant-jet (2%).

For 1-3 and 5, we used the same systematic errors as these estimated in the anti-tagged analysis (described in Section 6.4.2). Using the Monte-Carlo simulations, we estimated the uncertainty of 6 as the difference between two cases of generating remnant partons; one along the beam direction and the other with P_T of 0.44 GeV (Gaussian distribution) with respect to the beam axis. These systematic errors are summarized in Table 6.2.

P_T range (GeV)	0.4 - 0.5	0.5 - 0.6	0.6 - 0.8	0.8 - 1.1	1.1 - 1.5	1.5 - 3.0
ee $\rightarrow$ ee $\tau\tau$	1.4	1.5	2.8	4.5	6.1	14.0
ee $\rightarrow$ hadron	1.1	6.0	7.6	9.1	16.5	39.4
γ-conv. (V^0 statistic)	17.6	15.9	19.1	29.7	22.9	87.2
γ-conv. (η statistic)	8.5	5.5	7.0	13.1	14.6	56.6
γ-conv. (η systematic)	0.8	5.2	12.6	3.2	7.5	4.1
direct process	1.1	1.4	1.9	2.4	3.1	5.9
ee $\rightarrow$ eeee	2.4	0.7	4.1	2.3	41.1	23.5
cut dependence	17.4	13.8	13.1	11.9	26.8	11.4
dE/dx fitting	6.4	8.9	3.0	2.6	1.1	13.8
acceptance correction	5.8	6.2	5.9	9.2	22.0	41.3
Total	27.7	25.7	30.0	37.5	63.2	123.2

Table 7.1: Systematic errors. (Percentage final electron inclusive cross section in each P_T binning.)

7.4.3 Result

The transverse momentum(P_T) dependence of the inclusive electron cross sections for the resolved-photon processes was measured. The polar angles of the selected electrons were limited to $|\cos\theta| \leq 0.77$.

The measured cross sections are summarized in Tables 7.2 where the first errors are statistical and the second ones are systematic (as discussed below). The results are also shown in Fig.7.6 for the inclusive electron cross section as a function of the electron P_T. The errors in Fig. 7.6 include both of these errors added in quadrature.

The inclusive electron cross section of the subprocess (resolved-photon process) integrated over the intervals $0.4 \leq P_T \leq 3.0$ GeV and $|\cos\theta| \leq 0.77$ was measured to be

$$7.8 \pm 1.7 \text{ (stat.)} \pm 1.1 \text{ (sys.) pb.}$$

P_T range (GeV)	$d\sigma/dP_T$ (pb/GeV)
0.4 - 0.5	26.0 $\pm$ 11.4 $\pm$ 7.2
0.5 - 0.6	20.3 $\pm$ 8.3 $\pm$ 5.2
0.6 - 0.8	8.0 $\pm$ 3.0 $\pm$ 2.3
0.8 - 1.1	2.9 $\pm$ 1.7 $\pm$ 1.1
1.1 - 1.5	1.3 $\pm$ 1.1 $\pm$ 0.8
1.5 - 3.0	0.15 $\pm$ 0.23 $\pm$ 0.19
Total	7.8 $\pm$ 1.7 $\pm$ 1.1

Table 7.2: Measured inclusive electron cross section for $|\cos\theta| \leq 0.77$ at P_T bin, together with the total cross section integrated over the P_T region from 0.4 to 3.0 GeV.

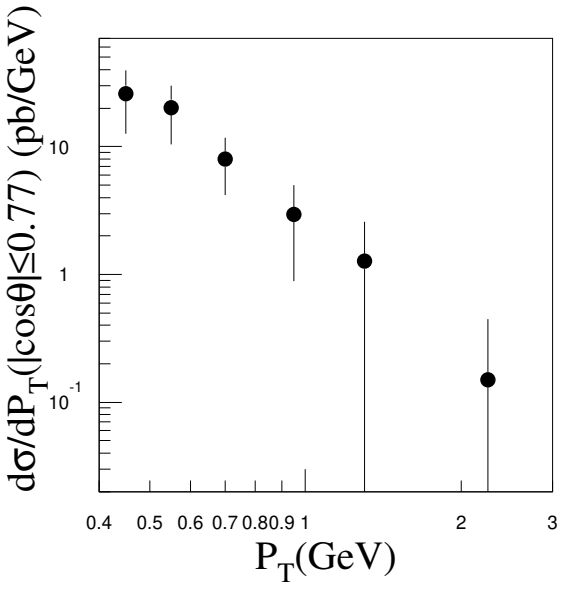

Figure 7.6: Differential cross section of inclusive electrons as a function of the electron-P_T in the remnant-jet-tag condition.

Chapter 8

Discussion

So far experimental studies of c-quark production in $\gamma\gamma$ collisions were carried out. The JADE collaboration, looked for fully reconstructed charged D^* mesons in single-tag events[60]. They reported a considerable excess over direct predictions, but this has not been confirmed by TASSO [61] or TPC/2γ [62] collaborations, who took data at similar energies. TASSO also measured the cross section for exclusive $D^0\overline{D^0}$ production. The total $c\bar{c}$ production cross-sections derived by these two experiments agreed with expectations[14].

The first study of charm production in two photon collisions at TRISTAN, by the TOPAZ collaboration [16], also searched for fully reconstructed D^* mesons. Since the reconstruction efficiency is quite low, leading to rather poor statistics (a few dozen events per experiment), they also studied D^* mesons using a soft-pion method[17]; where the signal after background subtraction consists of 372 ± 54 events. The VENUS collaboration have reported the c-quark study using the inclusive-electron methods[18]. After subtracting backgrounds, there remained 68 ± 11 electrons at relatively high-momentum range of $0.8 \leq P \leq 4.0$ GeV. These TRISTAN experiments found excess of events over the prediction of direct process.

However, most of these experimental analyses are only sensitive to charmed hadrons with high transverse momentum. On the other hand, our inclusive-electron analysis detected electrons with momentum as low as 400 MeV, so that low-P_T charm quarks can contribute to the signal significantly. The P_T and x distributions for tagged c-quarks in our inclusive-electron analysis are shown in Figs. 8.1-(a) and (b), respectively. As shown in the figures, we could access to the low-P_T region corresponding to the small-x region down to 0.02 where large difference between the parametrization appeared. This analysis was therefore sensitive to the difference in the parametrization of the parton densities in the photon.

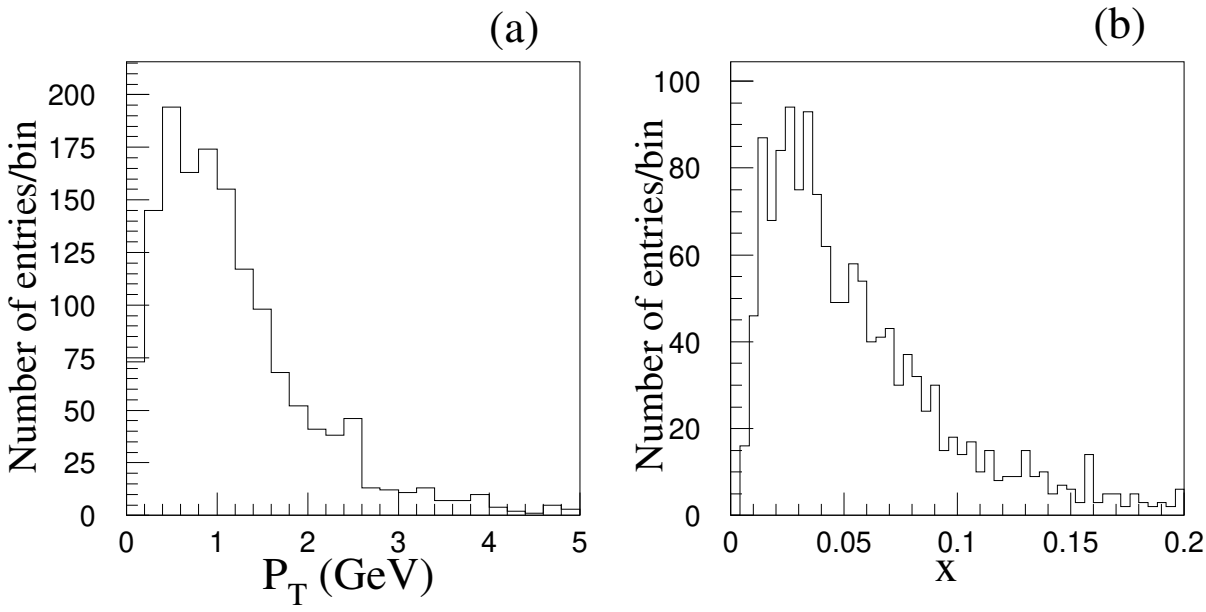

Figure 8.1: (a) P_T and (b) x distributions for c-quarks which were tagged by electrons, obtained by Monte-Carlo simulations.

Moreover, we used the forward calorimeter, which covers angles down to 3.2° , to look for the presence of remnant-jets in the event. The Monte-Carlo simulation study predicts a remnant-jet tagging efficiency of $73 \pm 2\%$. This allows us to study the resolved photon contribution separately.

The measured inclusive-electron cross sections in this analysis are compared with the theoretical predictions based on the direct and resolved-photon processes in Figs.8.2-(a) and (b), and the integrated cross sections are summarized in Table 8.1. Where we use LAC1 and DG parametrization in the figures and that of LAC1, DG, WHIT1, and WHIT4 in the table, for the resolved-photon process. The lowest-order(LO) predictions are shown in Fig.8.2-(a), while Fig.8.2-(b) shows the higher-order [next-to-leading-order(NLO)] predictions[14, 16, 17]. The NLO corrections increase the cross sections by about 31% for the direct process. The effects of the charm-quark mass are also shown in the two histograms of direct+LAC1 predictions in Figs. 8.2-(a) and (b) as well as in Table 8.1. From these figures and the table, it is clear that the direct process(solid histogram) alone falls short of the observed inclusive electron cross section, being consistent with the previous $D^{*\pm}$ analysis[16, 17] and inclusive-electron analysis by the VENUS[18].

The direct process alone cannot explain the remnant-jet activities, either. The subprocess cross sections obtained from the remnant-jet-tag sample are compared to the predictions from the resolved-photon processes in Figs. 8.3-(a) and (b) for

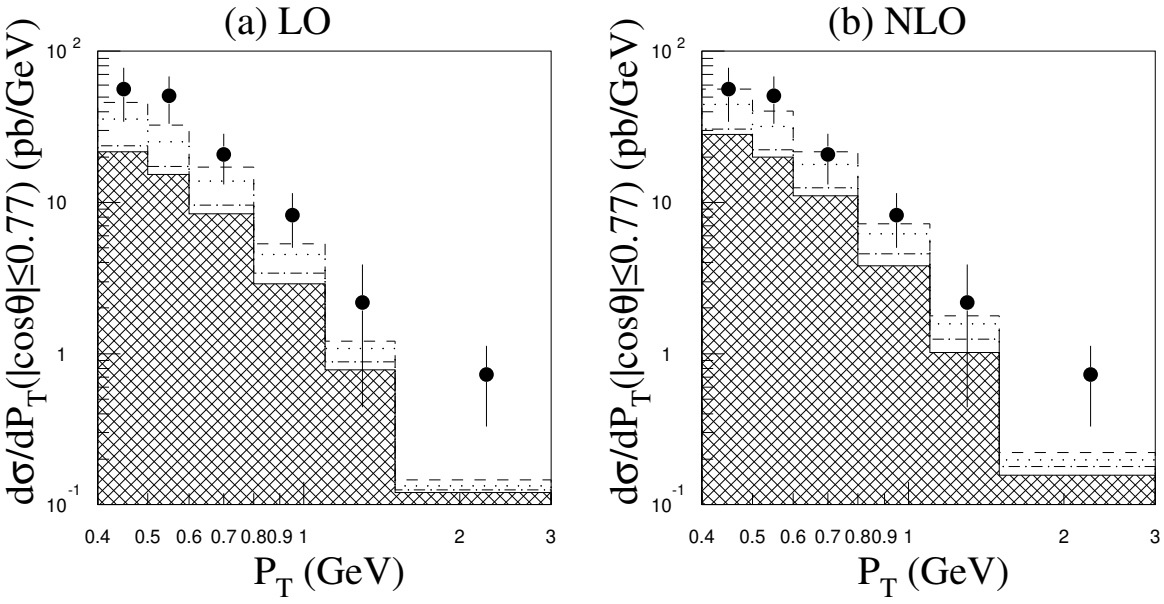

Figure 8.2: Differential cross section, $d\sigma/dP_T$ ($|\cos\theta| \leq 0.77$)(pb/GeV), of inclusive electrons for the electron-P_T, where anti-tag condition is imposed. The solid circles are the experimental data, while the histograms are the theoretical predictions of (a) LO and (b) NLO ; the hatched areas are the direct only, the dotdashed lines are the direct+DG, the dotted lines are the direct+LAC1 with a c-quark mass of 1.5GeV, and the dashed lines are the direct+LAC1 with a c-quark mass of 1.3GeV.

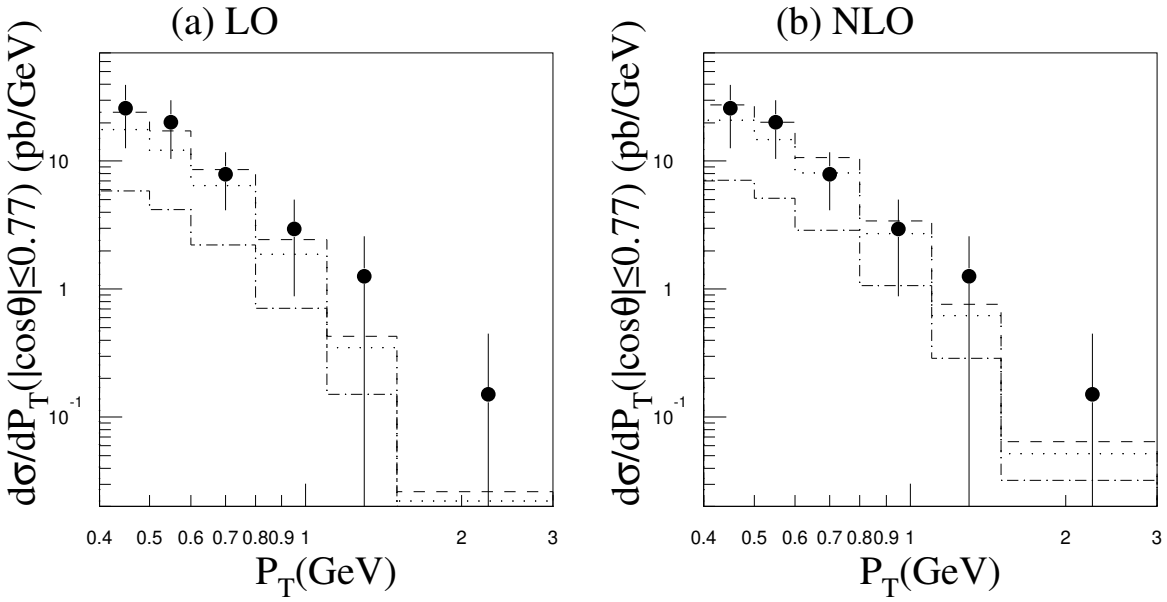

Figure 8.3: Differential cross section, $d\sigma/dP_T$ ($|\cos\theta| \leq 0.77$)(pb/GeV), of inclusive electrons for the electron-P_T obtained from the remnant-jet-tag sample. The solid circles are the experimental data, while the histograms are the theoretical predictions of (a) LO and (b) NLO ; the dotdashed lines are the DG, the dotted lines are the LAC1 with a c-quark mass of 1.5GeV, and the dashed lines are the LAC1 with a c-quark mass of 1.3GeV.

		anti-tag				remnant jet-tag			
σ_{data}	(pb)	19.3 ± 2.7 ± 2.1				7.8 ± 1.7 ± 1.1			
		LO		NLO		LO		NLO	
charm-quark mass	(GeV)	1.5	1.3	1.5	1.3	1.5	1.3	1.5	1.3
σ_{direct}		5.8	6.7	7.6	8.8	-	-	-	-
σ_{DG}		1.7	2.4	2.3	3.0	1.7	2.4	2.3	3.0
σ_{WHIT1}	(pb)	1.9	2.4	2.5	3.1	1.9	2.4	2.5	3.1
σ_{WHIT4}		3.3	4.1	4.2	5.1	3.3	4.1	4.2	5.1
σ_{LAC1}		5.0	6.8	6.3	8.3	5.0	6.8	6.3	8.3
$\sigma_{direct+DG}$		7.5	9.1	9.9	11.8	-	-	-	-
$\sigma_{direct+WHIT1}$	(pb)	7.7	9.1	10.1	11.9	-	-	-	-
$\sigma_{direct+WHIT4}$		9.1	10.8	11.8	13.9	-	-	-	-
$\sigma_{direct+LAC1}$		10.8	13.5	13.9	17.1	-	-	-	-

Table 8.1: Measured inclusive electron cross sections integrated over the P_T region from 0.4 to 3.0 GeV for $|\cos\theta| \leq 0.77$, together with the theoretical predictions based on the direct and resolved-photon processes. The dependence on the c-quark mass and the effect of the NLO corrections are also shown.

LO and NLO predictions, respectively. From this figure and Fig. 8.2, we can conclude that the data is explained with the prediction based on the LAC1/WHIT4 parametrization with including the NLO correction. Where the data agree better with the prediction assuming the low c-quark mass of 1.3 GeV. On the other hand, the DG/WHIT1 parametrization cannot explain the data even if the NLO corrections and the effect of the charm-quark mass is taken into account. As mentioned before, this inclusive electron measurement is sensitive to the difference in the parton distributions for the kinematical region of x down to 0.02. The difference in the predictions of LAC1/WHIT4 and DG/WHIT1 results mainly from the difference in the gluon distribution at small x less than 0.1. Our results indicate that the gluon content increases rather rapidly at the small-x region ($x < 0.1$).

Chapter 9

Conclusions

We have studied charm-quark productions in $\gamma\gamma$ collisions with the TOPAZ detector at the TRISTAN e^+e^- collider. In this study, charm quarks were identified by electrons (and positrons) from semi-leptonic decay of charm-quarks. The data corresponded to an integrated luminosity of 95 pb^{-1} at a center-of-mass energy ($\sqrt{s}$) of 58 GeV.

The inclusive electron cross sections imposing an anti-tag condition were measured. The subprocess cross sections for resolved-photon processes were also measured separately by using a remnant-jet-tag sample. The inclusive electron cross section integrated over the intervals $0.4 \leq P_T \leq 3.0$ GeV and $|\cos\theta| \leq 0.77$ was measured to be

$$19.1 \pm 2.7 \text{ (stat.)} \pm 2.1 \text{ (sys.) pb},$$

while that of the subprocess (resolved-photon process) over the same intervals was

$$7.9 \pm 1.7 \text{ (stat.)} \pm 1.1 \text{ (sys.) pb}.$$

The results were compared with the predictions of inclusive electron cross section based on the direct and resolved-photon processes. Here, in the predictions, the uncertainties caused by the charm-quark mass and the effect of the next-to-leading order corrections were studied. The direct process alone can explain neither the cross sections nor the remnant-jet activities. This study was sensitive to the difference in the parametrization of the parton densities in the photon, since we could access to the small-x region down to 0.02 where large difference between the parametrization appears. As the results, our data were well explained if the LAC1/WHIT4 parametrization including the NLO corrections, was taken for the parton distribution in a photon. This implies that there are relatively large gluon contents at small x in a photon. On the other hand, the DG/WHIT1

parametrization could not explain the data even if the NLO corrections and the effect of the charm-quark mass were taken into account.

Appendix A

Cross sections for the sub-processes

Here we summarize below the cross section formulae for the sub-processes. In these formulae, we represents the sub-process cross sections as differential cross sections of $\hat{\theta}$ which is the scattering angle in the center-of-mass system and mandelstarm variables of $\hat{s}$, $\hat{t}$ and $\hat{u}$. The suffixes for q indicate the quark flavour, e_q is a quark charge, and $\hat{\beta}$ is a quark velocity: $\hat{\beta} = \sqrt{1 - 4m_q^2/\hat{s}}$.

$\gamma\gamma \to q_i\bar{q}_i$

$$\begin{aligned}\frac{d\sigma}{d\cos\hat{\theta}} &= \frac{3\pi\alpha^2 e_q^4\hat{\beta}}{\hat{s}}\left[\frac{m_q^2-\hat{t}}{m_q^2-\hat{u}}+\frac{m_q^2-\hat{u}}{m_q^2-\hat{t}}+4\left(\frac{m_q^2}{m_q^2-\hat{t}}+\frac{m_q^2}{m_q^2-\hat{u}}\right)\right.\\ &- \left. 4\left(\frac{m_q^2}{m_q^2-\hat{t}}+\frac{m_q^2}{m_q^2-\hat{u}}\right)^2\right]. \qquad \text{(A.1)}\end{aligned}$$

$\gamma q_i \to q_i g$

$$\frac{d\sigma}{d\cos\hat{\theta}} = -\frac{4\pi\alpha e_q^2\alpha_S}{3\hat{s}}\left(\frac{\hat{t}}{\hat{s}}+\frac{\hat{s}}{\hat{t}}\right) \qquad \text{(A.2)}$$

$\gamma g \to q_i\bar{q}_i$

$$\begin{aligned}\frac{d\sigma}{d\cos\hat{\theta}} &= \frac{\pi\alpha e_q^2\alpha_S\hat{\beta}}{2\hat{s}}\left[\frac{m_q^2-\hat{t}}{m_q^2-\hat{u}}+\frac{m_q^2-\hat{u}}{m_q^2-\hat{t}}+4\left(\frac{m_q^2}{m_q^2-\hat{t}}+\frac{m_q^2}{m_q^2-\hat{u}}\right)\right.\\ &- \left. 4\left(\frac{m_q^2}{m_q^2-\hat{t}}+\frac{m_q^2}{m_q^2-\hat{u}}\right)^2\right]. \qquad \text{(A.3)}\end{aligned}$$

$q_i + q_i \to q_i + q_i$

$$\frac{d\sigma}{d\cos\hat{\theta}} = \frac{\pi\alpha_S^2}{4\hat{s}}\left[\frac{4}{9}\left(\frac{\hat{s}^2+\hat{u}^2}{\hat{t}^2}+\frac{\hat{s}^2+\hat{t}^2}{\hat{u}^2}\right)-\frac{8}{27}\frac{\hat{s}^2}{\hat{u}\hat{t}}\right] \tag{A.4}$$

$q_i + q_j \to q_i + q_j$

$$\frac{d\sigma}{d\cos\hat{\theta}} = \frac{\pi\alpha_S^2}{2\hat{s}}\left[\frac{4}{9}\frac{\hat{s}^2+\hat{u}^2}{\hat{t}^2}\right] \tag{A.5}$$

$q_i + \bar{q}_i \to q_i + \bar{q}_i$

$$\frac{d\sigma}{d\cos\hat{\theta}} = \frac{\pi\alpha_S^2}{2\hat{s}}\left[\frac{4}{9}\left(\frac{\hat{s}^2+\hat{u}^2}{\hat{t}^2}+\frac{\hat{t}^2+\hat{u}^2}{\hat{s}^2}\right)-\frac{8}{27}\frac{\hat{u}^2}{\hat{s}\hat{t}}\right] \tag{A.6}$$

$q_i + \bar{q}_i \to q_j + \bar{q}_j$

$$\frac{d\sigma}{d\cos\hat{\theta}} = \frac{\pi\alpha_S^2\hat{\beta}}{2\hat{s}}\frac{4}{9}\left[\frac{(m_q^2-\hat{t})^2+(m_q^2-\hat{u})^2+2m_q^2\hat{s}}{\hat{s}^2}\right] \tag{A.7}$$

$q_i + \bar{q}_j \to q_i + \bar{q}_j$

$$\frac{d\sigma}{d\cos\hat{\theta}} = \frac{\pi\alpha_S^2}{2\hat{s}}\frac{4}{9}\left[\frac{\hat{s}^2+\hat{u}^2}{\hat{t}^2}\right] \tag{A.8}$$

$q_i + \bar{q}_i \to g + g$

$$\frac{d\sigma}{d\cos\hat{\theta}} = \frac{\pi\alpha_S^2}{2\hat{s}}\left[\frac{32}{27}\frac{\hat{u}^2+\hat{t}^2}{\hat{u}\hat{t}}-\frac{8}{3}\frac{\hat{u}^2+\hat{t}^2}{\hat{s}^2}\right] \tag{A.9}$$

$q_i + g \to q_i + g$

$$\frac{d\sigma}{d\cos\hat{\theta}} = \frac{\pi\alpha_S^2}{2\hat{s}}\left[-\frac{4}{9}\frac{\hat{u}^2+\hat{s}^2}{\hat{u}\hat{s}}+\frac{\hat{u}^2+\hat{s}^2}{\hat{t}^2}\right] \tag{A.10}$$

$g + g \to q_i + \bar{q}_i$

$$\begin{aligned}
\frac{d\sigma}{d\cos\hat{\theta}} &= \frac{\pi\alpha_S^2\hat{\beta}}{32\hat{s}}\left[12\frac{(m_q^2-\hat{t})(m_q^2-\hat{u})}{\hat{s}^2}+\frac{8}{3}\frac{(m_q^2-\hat{t})(m_q^2-\hat{u})-2m_q^2(m_q^2+\hat{t})}{(m_q^2-\hat{t})^2}\right.\\
&+ \frac{8}{3}\frac{(m_q^2-\hat{t})(m_q^2-\hat{u})-2m_q^2(m_q^2+\hat{u})}{(m_q^2-\hat{u})^2}-\frac{2}{3}\frac{m_q^2(\hat{s}-4m_q^2)}{(m_q^2-\hat{t})(m_q^2-\hat{u})}\\
&- 6\frac{(m_q^2-\hat{t})(m_q^2-\hat{u})+m_q^2(\hat{u}-\hat{t})}{\hat{s}(m_q^2-\hat{t})}\\
&- \left.6\frac{(m_q^2-\hat{t})(m_q^2-\hat{u})+m_q^2(\hat{t}-\hat{u})}{\hat{s}(m_q^2-\hat{u})}\right] \qquad \text{(A.11)}
\end{aligned}$$

$g + g \to g + g$

$$\frac{d\sigma}{d\cos\hat{\theta}} = \frac{\pi\alpha_S^2}{4\hat{s}}\frac{9}{2}\left[3-\frac{\hat{u}\hat{t}}{\hat{s}^2}-\frac{\hat{u}\hat{s}}{\hat{t}^2}-\frac{\hat{s}\hat{t}}{\hat{u}^2}\right] \qquad \text{(A.12)}$$

Appendix B

Altarelli-Parisi splitting functions

In this appendix, we summarize the explicit formulae of the leading order (LO) Altarelli-Parisi splitting functions in the Fig. B.1. In the figure, $P_{ij}(x)$ is the $j \to i$ splitting function which represents the probability that the daughter parton i carries a fraction x of the momentum of the parent parton j.

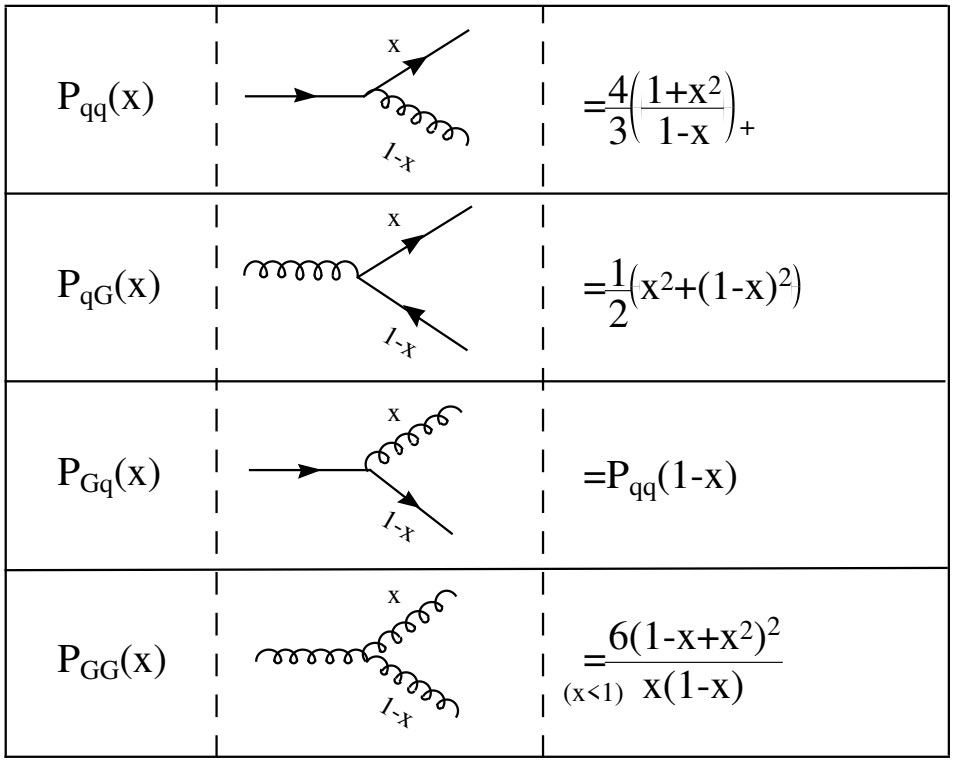

Figure B.1: Formulae of the leading order Altarelli-Parisi splitting functions.

Bibliography

[1] T. Kinoshita and W. B. Lindquist, Phys. Rev. Lett. **47** (1981) 1573.

[2] J. J. Sakurai and D. Schildknecht, Phys. Lett. **B40** (1979) 121; I. F. Ginzburg and V. G. Selbo, Phys. Lett. **B109** (1982) 231.

[3] M. Drees and R. M. Godbole, Nucl. Phys. **B339** (1990) 355.

[4] P. Aurenche *et. al.*, *Prog. Theor. Phys.* **92** (1994) 175.

[5] S. J. Broadsky, T. A. DeGrand, J. F. Gunion, and J. H. Weis, Phys. Rev. Lett. **41** (1978) 672, and Phys. Rev. **D19** (1979) 1418; G. H. Llewellyn-Smith, Phys. Lett. **79B** (1978) 83; H. Terazawa, J. Phys. Soc. of Japan, **47** (1979) 355; K. Kajantie and R. Raitio, Nucl. Phys. **B159** (1979) 528.

[6] PLUTO Collab., Ch. Berger *et. al.*, Z. Phys. **C29** (1985) 499; Z. Phys. **C33** (1987) 351.

[7] TPC/2γ Collab., H. Aihara *et.al.*,Phys. ReV. **D41** (1990) 2667.

[8] CELLO Collab., H. j. Behrend *et.al.*, Z. Phys. **C51** (1991) 365.

[9] AMY Collab., R. Tanaka it et.al., Phys. Lett. **B277** (1992) 215.

[10] TOPAZ Collab., H. Hayashii *et.al.*, Phys. Lett. **B314** (1993) 149.

[11] B.J. Kim *et.al.*, Phys.Lett. **B325** (1994) 248.

[12] H1 Collab., T. Ahmed *et.al.*, Phys. Lett. **B297** (1992) 205;
ZEUS Collab., M. Derrick *et.al.*, Phys. Lett. **B297** (1992) 404.

[13] H. Abramowicz, K. Charchula, and A. Levy, Phys. Lett. **B269** (1991) 458.

[14] M. Drees, M. Kämer, J. Zunft, and P. M. Zerwas, Phys. Lett. **B306** (1993) 371; J. Smith and W. van. Neerven, Nucl. Phys. **274** (1992) 36.

[15] TASSO Collab., W. Braunschweig *et.al.*, Z. Phys. **C47** (1990) 499;
TPC/2γ Collab. M. Alston-Garnjost *et.al.*, Phys. Lett. **B252** (1990) 499.

[16] TOPAZ Collab., R. Enomoto et. al., Phys. Rev. **D50** (1994) 1879;

[17] TOPAZ Collab., R. Enomoto et. al., Phys. Lett. **B328** (1994) 535.

[18] VENUS Collab., S. Uehara et. al., Z. Phys. **C63** (1994) 213.

[19] M. Drees and K. Grassie, Z. Phys. **C28** (1985) 451.

[20] M. Glück, E. Reya, and A. Vogt, Phys. Rev. **D46** (1992) 1973.

[21] P. Aurenche, P. Chiappeta, M. Fontannaz, J. P. Guillet and E. Pilon, Z. Phys. **C56** (1992) 589.

[22] L. E. Gordon and J. K. Storrow, Z. Phys., **C56** (1992) 307.

[23] H. Hagiwara, M. Tanaka, I. Watanabe, and T. Izubuchi, *Phys. Rev.* **D51** (1995) 3197.

[24] Particle Data Group, M. Aguilar-Benitez*et. al.*, *Phys. Rev.* **D50** (1994) 1173.

[25] C. Weizäcker, Z. Phys. **88** (1934) 612; E. J. Williams, Phys. Rev. **45** (1934) 729.

[26] K. Hagiwara, H. Iwasaki, A. Miyamoto, H. Murayama and D. Zeppenfeld, Nucl. Phys. **B365** (1991) 544.

[27] S. Frixione, M. L. Mangano, P. Nason, and G. Ridolfi Phys. Lett. **B319** (1993) 339.

[28] M. Kuroda, Meiji Gakuin University (Tokyo) Research J. 424 (1988)27.

[29] M. Glück and E. Reya, Phys. Rev. **D28** (1983) 2749.

[30] E. Witten, Nucl. Phys. **B120** (1977) 189;
R. J. deWitt, L. M. Jones, J. D. Sullivan, D. E. Willen, and H. W. Wyld, Phys. Rev. **D19** (1979) 2046.

[31] G. Altareli and G. Parisi, Nucl. Phys. **B126** (1977) 298.

[32] PLUTO Collab., Ch. Berger *et. al.*, Z. Phys. **C26** (1984) 191; Z. Phys. **C29** (1985) 499.

[33] J. L. Rosner, Brookhaven Report CRISP 7126 (1971).

[34] S. J. Broadsky, T. Kinoshita, and H. Terazawa, Phys. Rev. **D4** (1971) 1532.

[35] V. Fadin, V. A. Khoze, and T. Sjöstrand,Z. Phys. **C48** (1990) 613.

[36] M. Glück, J. F. Owens, and E. Reya, Phys. Rev. **D17** (1978) 2324.

[37] R. Hayano et al., TRISTAN-EXP-002 (1983).

[38] T. Kamae et al., Nucl. Instrum. Meth., **A 252** (1986) 423.

[39] H. Kichimi *et.al.*, Nucl. Instrum. Meth. **A334** (1993) 367.

[40] S. Kawabata et al., Nucl. Instrum. Meth. **A 270** (1988) 419.

[41] K. Fujii *et. al.*, Nucl. Instrum. Meth. **A236** (1985) 55; J. Fujimoto, *et. al.*, Nucl. Instrum. Meth. **A256** (1987) 449.

[42] H.Hayashii *et. al.*, Nucl. Instrum. Meth. **A316** (1992) 202.

[43] S. Noguchi et al., Nucl. Instrum. Meth., **A 271** (1988) 464

[44] R. Enomoto et al., Nucl. Instrum. Meth., **A 269** (1988) 507; R. Enomoto, K. Tsukada, N. Ujiie, and A. Shirahashi, IEEE trans. NS. **Vol. 35, No. 1** (1988) 419; T. Tsukamoto, M. Yamauchi, and R. Enomoto, Nucl. Instrum. Meth. **A 297** (1990) 148.

[45] K. Fujii et al., Nucl. Instrum. Meth., **A 264** (1988) 297.

[46] A. Shirahashi et al., IEEE Trans. Nucl. Sci. **35** (1988) 414.

[47] W. Nelson, H. Hirayama, and D. Rogers, SLAC-Report-265 (1987), unpublished.

[48] K. Ogawa et al., KEK internal Report, 85-2 (1985).

[49] S. Kawabata, Comp. Phys. Comm., **41** (1986) 127.

[50] T. Sjöstrand, Comp. phys. Comm., **39** (1986) 347; T.Sjöstrand and M.Bengtsson, Comp. phys. Comm., **43** (1987) 367.

[51] R. Itoh et al., IEEE Trans. on Nucl. Sci. **NS-34** (1987) 533.

[52] W. Nelson, H. Hirayama, and D. Rogers, SLAC-Report-265 (1987), unpublished.

[53] E. Longo and L. Luminari, Nucl. Instrum. Meth. **A 239** (1985) 506.

[54] H. Fesefeldt, PITHA 85/02 (1985)

[55] TOPAZ collab., K. Nagai *et. al.*, Phys. Lett. **B278** (1992) 506.

[56] TOPAZ collab., I. Adachi *et. al.*, Phys. Lett. **B227** (1989) 495.

[57] TOPAZ collab., H. Hayashii *et. al.*, Phys. Lett. **B279** (1992) 422.

[58] TOPAZ collab., B. Howell *et. al.*, Phys. Lett. **B291** (1992) 206.

[59] T. Tauchi, KEK-preprint, KEK-94-67, to be appeared in the proceedings of XXIXth Recontres de Moriond "QCD and High Energy Interactions", Meribel, France, March 19-26, 1994.

[60] JADE collab., W. Bartel et al., Phys. Lett. **B184**, 288 (1987).

[61] TASSO collab., W. Braunschweig et al., Z. Phys. **C47**, 499 (1990).

[62] TPC/2γ collab., M. Alston–Garnjost et al., Phys. Lett. **B252**, 499 (1990).